ANNALS OF GEOPHYSICS, 67, 2, PA218, 2024; doi:10.4401/ag-9117
OPEN ACCESS

The effects of the May 2024 Mother's Day superstorm over the Mediterranean sector: from data to public communication

Luca Spogli[*,1], Tommaso Alberti[1], Paolo Bagiacchi[1], Lili Cafarella[1], Claudio Cesaroni[1], Gianfranco Cianchini[1], Igino Coco[1], Domenico Di Mauro[1], Rebecca Ghidoni[2,1], Fabio Giannattasio[1], Alessandro Ippolito[1], Carlo Marcocci[1], Michael Pezzopane[1], Emanuele Pica[1], Alessio Pignalberi[1], Loredana Perrone[1], Vincenzo Romano[1], Dario Sabbagh[1], Carlo Scotto[1], Sabina Spadoni[1], Roberta Tozzi[1], Massimo Viola[1]

(1) Istituto Nazionale di Geofisica e Vulcanologia, Rome, Italy
(2) Alma Mater Studiorum – Università degli studi di Bologna, Bologna, Italy

Article history: received June 3, 2024; accepted June 20, 2024

Abstract

On 8 May 2024, the solar active region AR13664 started releasing a series of intense solar flares. Those of class X released between 9 and 11 May 2024 gave rise to a chain of fast Coronal Mass Ejections (CMEs) that proved to be geoeffective. The Storm Sudden Commencement (SSC) of the resulting geomagnetic storm was registered on 10 May 2024 and it is, to date, the strongest event since November 2003. The May 2024 storm, named hereafter Mother's Day storm, peaked with a Dst of −412 nT and stands out as a "standard candle" storm affecting modern era technologies prone to Space Weather threats. Moreover, the recovery phase exhibited almost no substorm signatures, making the Mother's Day storm as a perfect storm example. Despite the plethora of notable near-Earth environment modifications that are still under investigation, in this paper we concentrate on the Space Weather effects over the Mediterranean sector, with a focus on Italy. In fact, the Istituto Nazionale di Geofisica e Vulcanologia (INGV) manages a dense network of GNSS receivers (including scintillation receivers), ionosondes and magnetometers in the Mediterranean area, which facilitated for a detailed characterization of the modifications induced by the storm. Concerning the geomagnetic field, observatories located in Italy recorded a SSC with a rise time of only 3 minutes and a maximum variation of around 600 nT. The most notable ionospheric effect following the arrival of the disturbance was a significant decrease in plasma density on 11 May, resulting in a pronounced negative ionospheric storm registered on both the critical F2-layer frequency (*fo*F2) and the Total Electron Content (TEC). Another negative effect was recorded on 13 May, while no signatures of positive storm phases were reported. These negative ionospheric phases are ascribed to neutral composition changes and, specifically, to a decrease of the $[O]/[N_2]$ ratio. The IRI UP IONORING data-assimilation procedure, recently developed to nowcast *fo*F2 over Italy, proved to be quite reliable during this extreme event, being characterised just by an overestimation during the main phase of the storm, when the electron density and the height of the F region decreased and increased, respectively. Relevant outcomes of the work relate to the Rate Of TEC change Index (ROTI), which shows unusually high spatially distributed values on the nights of 10 and 11 May. The ROTI enhancements on 10 May might be linked to Stable Auroral Red (SAR) arcs and an equatorward displacement of the main ionospheric trough. Instead, the ROTI enhancements on 11 May might be triggered by

a joint action of low-latitude plasma pushed poleward by the pre-reversal enhancement (PRE) in the post-sunset hours and wave-like perturbations propagating from the North. Furthermore, the storm generated immediate attention of the general public to Space Weather effects, including mid-latitude visible phenomena like SAR arcs. This paper outlines the report of the Space Weather Monitoring Group (SWMG) of the INGV Environment Department and its effort to disseminate information about this exceptional event.

Keywords: Extreme geomagnetic storm; Ionospheric storm; Mid-latitude ionosphere; Ionospheric irregularities; Communication

1. Introduction

Finally, it happened! The Space Weather community has been waiting for an event like the 2024 Mother's Day storm for two decades. Twenty years ago, the 2003 Halloween series of events [Tsurutani et al., 2006; Lopez et al., 2004] and the November 2003 storm [Gopalswamy et al., 2005; Srivastava et al., 2009] opened a new era, in which modern society started realising its exposure to Space Weather threats and new opportunities for awareness were realised. Then, solar cycle 24th, despite predictions, was less intense, as it was associated with fewer interesting storm events than expected. Among them, the St. Patrick's Day 2015 Storm [Astafyeva et al., 2015; Nava et al., 2016; Spogli et al., 2016; Perrone and Mikhailov, 2018], the June 2015 storm [Piersanti et al., 2017; Astafyeva et al., 2017; Cherniak and Zakharenkova, 2017], the September 2017 storm [Linty et al., 2018; Qian et al., 2019], the August 2018 storm [Spogli et al., 2022; Astafyeva et al., 2022] and the November 2021 storm [Regi et al., 2022; Kim et al., 2023] were characteristic case studies for Space Weather scientific investigation and an opportunity to test related services and models. However, such an extreme event like the Mother's Day storm was an exceptional scenario we were all waiting for. For what concerns the naming of the storm we decided to follow the recommendation made by the Executive Board of the European Space Weather and Space Climate Association (E-SWAN), which has recently suggested "Mother's Day" as a possible name to identify this specific storm (https://eswan.eu/index.php/newsletter/archive?view=article&id=200).

The Mother's Day storm offers the opportunity to improve our understanding of ionospheric dynamics in this region that is crucial due to its diverse geographical and geomagnetic characteristics, as well as its significant implications for various socio-economic activities. The Mediterranean region has specific needs in terms of Space Weather that cannot be addressed by global products or services, or by the local products that address high or low latitudes. Geomagnetic and ionospheric disturbances need to be monitored and evaluated by ground based local sensors in order to assess the Space Weather impact on the region. With regard to this, there is an increasing attention to the effect of solar, geomagnetic and ionospheric storms at mid latitudes [see, e.g., Mrak et al., 2023; Rodrigues et al., 2021; Tozzi et al., 2019; Watson and Pedatella, 2018]. Several institutions such as the International Civil Aviation Organization (ICAO) and the European Space Agency (ESA) have a special interest in this respect. ICAO identifies the high frequency (HF) and global navigation satellite system (GNSS) technologies potentially affected by extreme Space Weather events [Kauristie et al., 2021]. To mitigate such risk, ICAO selected regional and global centres to generate alerts in support of civil aviation. ESA has promoted the project "Space Weather User Needs for the Mediterranean Region'' in the frame of the Space Situational Awareness Programme (in response to ESA ITT Reference AO/1-9408/18/D/CT) and now, several mediterranean monitoring products are included in the ESA Space Weather Service Network (https://swe.ssa.esa.int/current-space-weather).

Bearing this in mind, the analysis here reported aims at investigating the solar and geospace conditions during the storm and to highlight the ionospheric and geomagnetic effects over the Mediterranean area, with a specific focus over Italy. The Istituto Nazionale di Geofisica e Vulcanologia (INGV) has a long tradition of ionospheric and geomagnetic monitoring, from which it is possible to derive a detailed and thorough characterization of the storm impact. Moreover, since 2022, INGV provides a Space Weather information and communication public service, through multiple activities conducted by the Space Weather Monitoring Group (SWMG) of the INGV Environment Department. This enables increasing our understanding of the impact of Space Weather and how this is perceived by

the general public. In view of this, the aim of this paper is to stress the importance of the following conceptual chain in serving the society as Space Weather scientists: monitoring phenomena, understanding physics, communicating science.

The paper is structured as follows: Section 2 provides the characterisation of the Mother's Day series of Space Weather events, by focusing on the source regions, the modification induced in the Interplanetary Magnetic Field (IMF) and Solar Wind (SW), and its global effect on the ground in terms of either global or regional activity indicators. Section 3 details the data and methodologies adopted to study the effects over the Mediterranean sector. Section 4 provides the results and the related discussion. Section 5 reports on the experience with public communication and conclusions are then drawn in Section 6.

2. The Mother's Day series of Space Weather events

The Mother's Day Space Weather events described in this work originated from the solar active region classified, by the National Oceanic Atmospheric Administration (NOAA), as AR13664. In the early hours of 8 May 2024, the region AR13664 was located at 18°S latitude and 17°W longitude (S18W17) in heliographic coordinates, and was characterised by a $\beta\gamma\delta$ configuration according to the Hale class, which is assigned to active regions with two sunspots or sunspot groups of opposite intermixed polarity that exhibit a complex topology. This active region generated several flares. Solar flares represent a release of magnetic energy detectable as a brightening in emission across the full electromagnetic spectrum [Benz, 2017; Fletcher et al., 2011]. They are induced by magnetic reconnection in the solar corona triggered by the eruption of a filament or a flux rope [Hirayama, 1974; Shibata et al., 1995]. The flare eruption involves sudden bursts of particle acceleration, plasma heating, and bulk mass motion. Following the flare classification according to their brightness in the wavelength range 1 to 8 Å, the X-class ones are the most powerful and significant solar flares. They are often related to Coronal Mass Ejections (CMEs), which are large expulsions of plasma and magnetic fields from the Sun's corona. CMEs associated with large X-ray flares are likely to be fast and wide [Gosling et al., 1976]. On 8 May 2024 AR13664 generated at least four M-class flares and one X1.0 flare, which started at 04:37 UT, reached its maximum at 05:09 UT and ended at 05:32 UT. It was the beginning of the strong activity in AR13664 that lasted for a few days. Figure 1 shows the full-disc continuum image (left panel) and the corresponding magnetogram (right panel) of AR13664 acquired by the Helioseismic and Magnetic Imager (HMI) [Scherrer et al., 2012] onboard the Solar Dynamic Observatory (SDO) mission [Pesnell et al., 2012] at the peak of

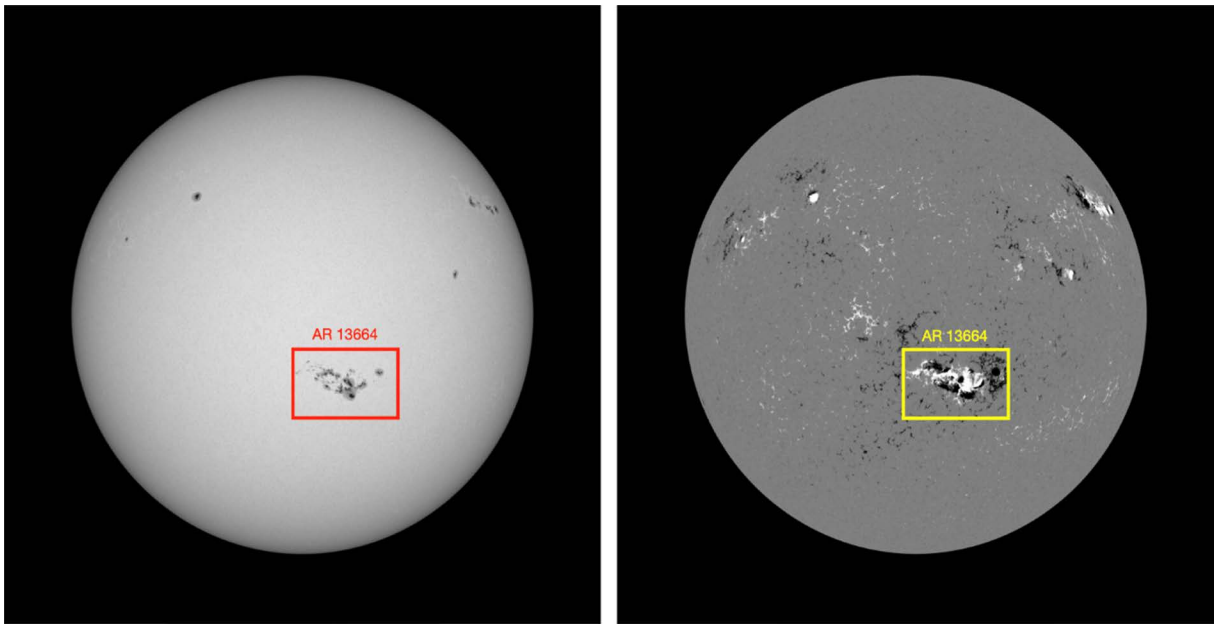

Figure 1. Full-disc continuum image (left panel) and the corresponding magnetogram (right panel) of AR13664 acquired by SDO/HMI on 8 May 2024. The rectangles in both panels mark the active region AR13664.

the X1.0 flare on 8 May. Images are acquired in the Fe I spectral line at 6173 Å with a 1'' spatial resolution, which corresponds to 725 km on the solar surface.

Subsequently, between the 9 and 11 May 2024 a number of solar flares of class X from AR13664 gave rise to a chain of fast CMEs responsible for the triggering and persistence of the strong Mother's Day geomagnetic storm. Figure 2 reports, between 9 May at 12:00 UT and 14 May, the conditions of the IMF and SW, and the global geomagnetic conditions expressed in terms of the quantities reported hereafter: X-ray flux (Fig. 2a) and ≥ 10 MeV proton flux (Fig. 2b) as measured by the Geostationary Operational Environmental Satellites (GOES) 16; total intensity B and Bz component of IMF (Fig. 2c), SW speed and density (Fig. 2d), and temperature (Fig. 2e) as measured by the Deep Space Climate Observatory (DSCOVR) satellite mission; electrojet indicators IE, IL and IU over the European Sector (Fig. 2f) provided by the International Monitor for Auroral Geomagnetic Effects (IMAGE) network of magnetometers [Tanskanen et al., 2009]; Kp index and Dst index (Fig. 2g). For what concerns IE, IU, and IL, only the magnetometers in the Finland sector, Northern Norway and Estonia were available (stations: KEV, MAS, KIL, MUO, IVA, PEL, RAN, OUJ, MEK, HAN, NUR, TAR), while, at the time of the writing, no data were available for 14 May 2024. From the X-ray flux measured by GOES and reported in Figure 2a, the intense solar activity of such days can be reconstructed, and it is found to be characterised by 5 X-class flares. This intense solar activity led to several CMEs, the most significant of which are probably related to the X-class flares observed. In Table 1, we outline the main characteristics of such CMEs, as described in the Computer Aided CME Tracking software (CACTus) catalogue [Robbrecht and Berghmans, 2004], and the potentially related solar flares.

CME Onset Time (UT)	Principal angle (counterclockwise from North; degrees)	Angular width (degrees)	Median velocity (km/s)	Maximum velocity (km/s)	Associated Flare
09/05/2024 09:24	237	132	1359	1785	X2.2
09/05/2024 19:24	051	020	649	1909	X1.1
10/05/2024 07:12	269	100	637	919	X4.0
11/05/2024 01:48	218	026	509	2015	X5.8
11/05/2024 02:36	021	344	1157	2015	X5.8
11/05/2024 17:24	212	162	509	1742	X1.5

Table 1. Main features of the CMEs related to the Mother's Day storm.

Ions of solar origin can be accelerated in a short time up to energies of 10 MeV to 1 GeV, in CME-driven shock waves or in strong solar flares [Ippolito et al., 2005; Reames, 2013]. During the strong solar events, which preceded the Mother's Day geomagnetic storm, solar proton fluxes remarkably increased as measured by the GOES-16 satellite and reported in Fig. 2b. The fluxes of solar protons with energy greater than 10 MeV show several enhancements due to the chain of solar events that occurred during the first half of May 2024, reaching the maximum of the peak on 11 May.

To investigate the IMF behaviour and SW plasma parameters, we used data collected by the DSCOVR spacecraft [Burt and Smith, 2012] located at the Lagrangian point L1, which provides real-time data on SW parameters and the IMF [Loto'aniu et al., 2022]. It collects plasma parameters (density, velocity, and temperature) at 1-minute resolution, as well as IMF measurements at 1-second resolution. The IMF behaviour and the SW plasma parameters (Figs. 2c-e) show the typical signature of an Interplanetary CME (ICME) detection [Gopalswamy, 2006]. Indeed, on 10 May 2024 at 16:40 UT a sudden increase was observed in speed (from 450 to 700 km/s), density (from 5 cm^{-3} to 40 cm^{-3}), and temperature (from 61000 K to 540000 K). This significant increase in SW speed corresponds to the leading edge of the ICME, while the sharp increase observed in the solar wind density and temperature is the signature of the

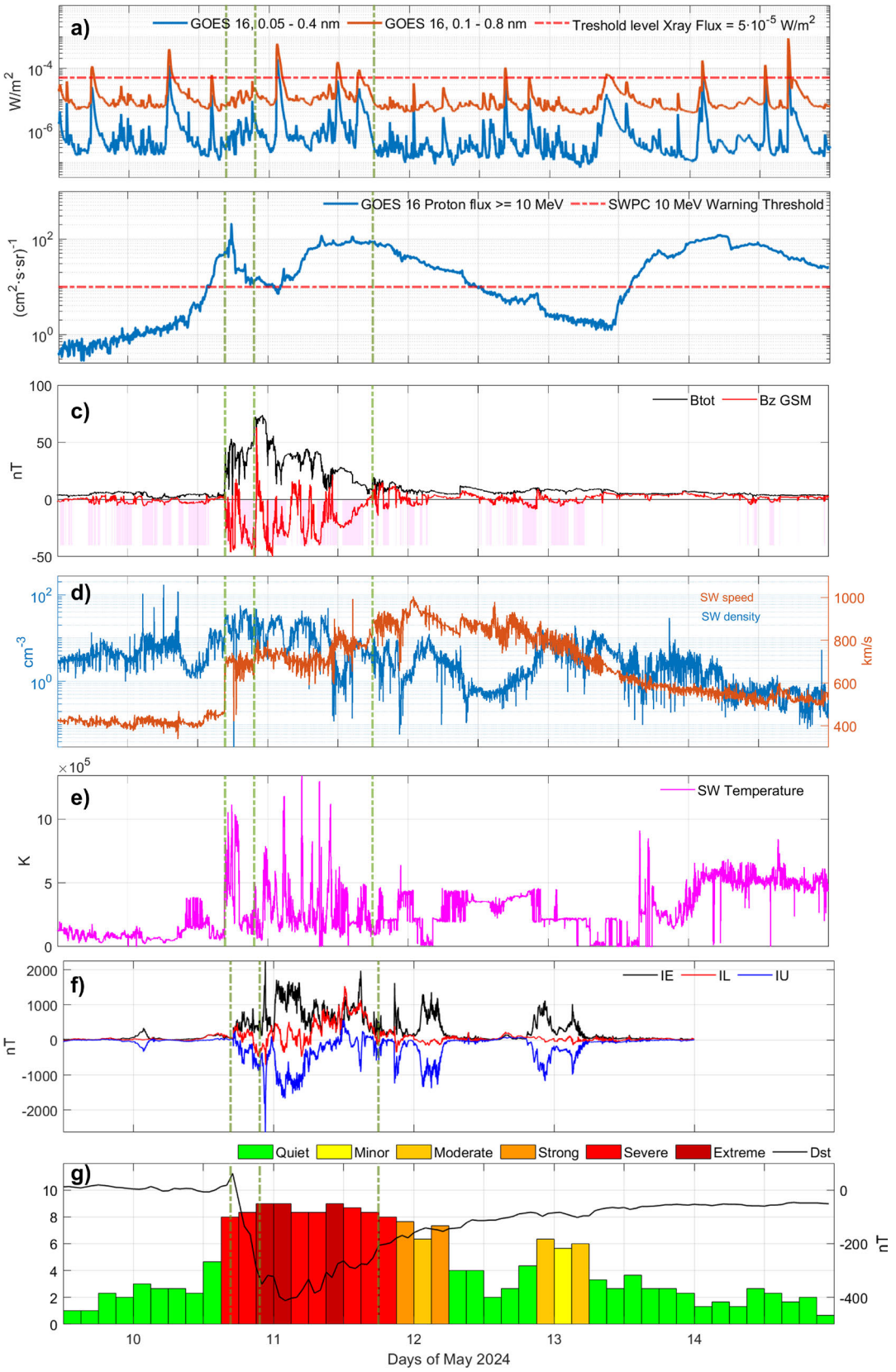

Figure 2. X-ray flux (panel a) and ≥ 10 MeV proton flux (panel b) as measured by GOES 16. Total intensity B and Bz component of IMF (panel c), SW speed and density (panel d), and temperature (panel e) as measured by DSCOVR satellite mission. IMAGE electrojet indicators IE, IL and IU (panel f). Kp index and Dst index (panel g), in which the colour code in panel indicates the NOAA Space Weather Scale for geomagnetic storms (https://www.swpc.noaa.gov/noaa-scales-explanation). The green dashed lines indicate the arrival of the shocks. Data cover the period from 9 May 2024 12:00 UT to 14 May 2024 23:59 UT.

shock front due to the compression and heating of the plasma [Gopalswamy, 2006]. Simultaneously, there is a switch towards large negative values of the IMF Bz, lasting for more than one day. This is associated with the presence of a magnetic cloud, with the magnetic field lines twisting within the ICME. Furthermore, an initial increase in the total magnetic field strength B is also clear, followed by successive increases, indicating the passage of additional ICMEs. Indeed, a second shock was observed at 21:39 UT of the same day, with the SW speed peaking close to 800 km/s, the IMF reaching 74 nT, and the Bz component falling to −50 nT. These shocks were linked to CMEs observed on 8-9 May, and possibly two to four associated ICMEs arrived at Earth between 10 and 11 May. A third shock-like structure was detected around 17:55 UT on 11 May, with the IMF strength jumping up to about 20 nT and SW speed increasing to 895 km/s. With the arrival of multiple ICMEs and High-Speed Streams (HSSs), the SW speed reached its peak value at nearly 1000 km/s at 00:55 UT on 12 May. Furthermore, a fourth shock-like structure was noted at 08:59 UT on 12 May, with a relatively small IMF increase from 5 nT to 12 nT and SW speed from 830 km/s to 900 km/s. These shocks were likely related to ICMEs passages from 9 to 11 May. However, on 12 May, Bz just returned to standard values characterised by small fluctuations around 0 nT, with the total intensity significantly reduced at about 8 nT. The long-lasting and strong Southward Bz component favoured the magnetic field reconnection at the flanks of the Earth's magnetopause, leading to the strongest geomagnetic storm in the last two decades.

According to the Dst index [Mayaud, 1980], on Earth, the storm began at 17:00 UT on 10 May 2024 with a SSC characterised by an amplitude of 44 nT (Fig. 2g). It is right the enhancement of the magnetopause currents that caused the observed SSC. Then, due to the growth of the ring current, the Dst index began its rapid decrease towards the geomagnetic storm main phase that ended when Dst reached the value of −412 nT. After that, the Dst index gradually recovered to its pre-storm values. Between the occurrence of the SSC and around 18:00 UT of 11 May, the Dst index exhibits an oscillating behaviour. By closely looking at these oscillations, it is possible to relate them to IMF Bz variations and to the shocks described above. In detail, increases in Dst seem to occur either when IMF Bz is positive and, hence, in a configuration of a closed magnetosphere or when abrupt variations in SW speed and density occur. On the other hand, Dst decreases seem to be related to negative IMF Bz, i.e., when the magnetosphere is in an open configuration. Some small variations are also present after 18:00 UT of 11 May, in a configuration of IMF Bz not favourable to reconnection (i.e., positive or near 0); these could be ascribed to the variations in SW density and speed observed in this time interval.

A behaviour analogous to that of Dst is displayed by the Kp index [Matzka et al., 2021]. We recall that Kp is a geomagnetic index estimated using data from 11 Northern and 2 Southern observatories located at (either Northern or Southern) geomagnetic latitudes between 44° and 60° and is used to measure the global geomagnetic activity over 3-hour intervals, with values ranging between 0^0 and 9. Kp index indicated strong geomagnetic activity on 10 May 2024 in the interval 12-15 UT when it reached the value of 5^-. In the following 3 hours, Kp rose up to 8^0 and then began oscillating between 8^0 and 9^0 until the late evening of 11 May 2024. It is interesting to observe that, while the Dst index started its recovery around 02:30 UT on 10 May 2024, Kp index did not. This can be explained by examining the behaviour of the IMAGE electrojet indicators IE, IL and IU. These indicators are calculated using the same procedure used for AE, AL and AU indices [Mayaud, 1980] but, due to the geographical position of contributing observatories, provide information on magnetic field perturbations induced by local auroral electrojet activity only in the European sector (more information available at https://space.fmi.fi/image/www/index.php?page=home). Figure 2f shows that these indicators depict perturbed values throughout the storm recovery phase and also between 12 and 13 May 2024, thus indicating notable auroral activity which is reflected in the Kp index.

3. Data and methods

This section describes the datasets adopted and how they were treated and used for the proposed analyses. Among them, those explicitly owned or managed by INGV are part of the electronic Space Weather upper atmosphere (eSWua, www.eswua.ingv.it) data portal [Pica et al., 2021] and the geomagnetic data portal (geomag.rm.ingv.it). Figure 3 shows the locations of the INGV observatories and measuring stations, comprising the INGV Space Weather monitoring service over the Mediterranean area. These include: GNSS Ionospheric Scintillation Monitor Receivers (ISMRs, green stars), the Advanced Ionospheric Sounder (AIS) ionosondes (red diamonds), the geomagnetic observatories and stations (blue squares) and the GNSS receivers constituting the Rete Integrata Nazionale GNSS (RING, http://ring.gm.ingv.it/) network (orange circles). Additionally, a subset of the EUREF Permanent GNSS Network (magenta circles) was also used. Each of these datasets are investigated in the following subsections.

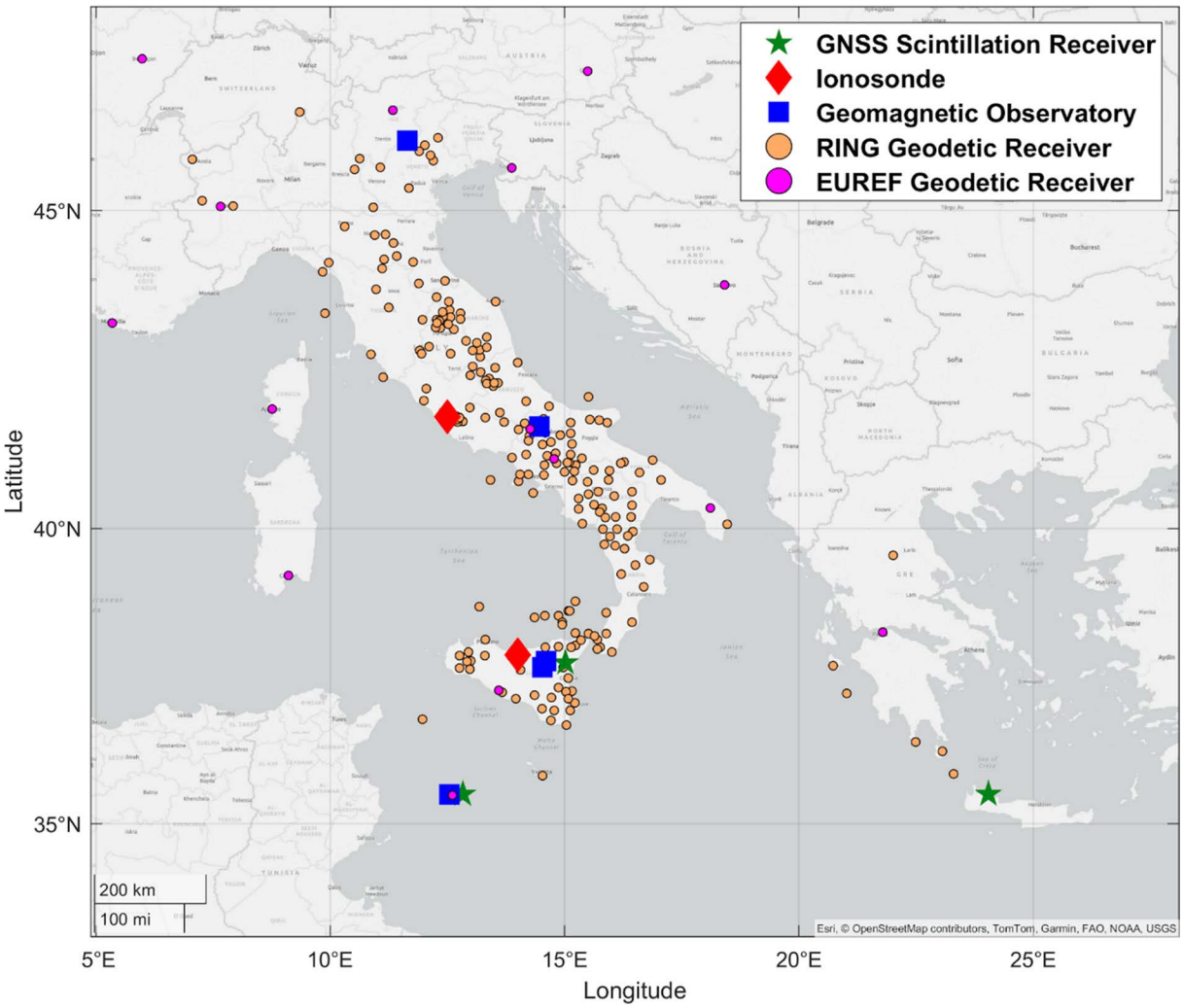

Figure 3. Locations of the INGV observatories and measuring stations comprising the INGV Space Weather monitoring service over the Mediterranean area and the selected GNSS receivers from the EUREF network.

3.1 Ionosondes

Ionosonde data over Italy were analysed to investigate the ionospheric response of the F region. The ionosondes in Rome (41.8°N, 12.5°E) and Gibilmanna (37.9°N, 14.0°E) (red diamonds in Fig. 3) are INGV Advanced Ionospheric Sounders (AIS-INGV) [Zuccheretti et al., 2003] and provide data in real-time by automatic interpretation using *Autoscala* scaling program of ionograms [Scotto, 2009; Scotto and Pezzopane, 2002], routinely recorded in digital format [Upper atmosphere physics and radiopropagation Working Group, 2020a]. Manually scaled data, curated by an experienced operator, are also available for retrospective studies [Upper atmosphere physics and radiopropagation Working Group, 2020b].

To analyse this storm, we used values of the critical frequency of the F2 layer (*fo*F2) manually scaled through the *Interpre* software [Pezzopane, 2004] from ionograms recorded every 15 minutes at both observatories, in comparison with the hourly medians of the manually scaled values in the 27 days preceding the 9 May. This was done to investigate in detail the variations in the ionisation at the peak in response to the storm, as *fo*F2 is strictly related to the maximum electron density in the F2 layer (*Nm*F2) through the plasma frequency formula.

Automatically scaled values of the peak altitude *hm*F2 were also used, after manually excluding unreasonable values. This was made by comparing the vertical electron density profile *Ne*(*h*), retrieved in the autoscaling procedure by the ionogram inversion [Scotto, 2009], to the recorded ionogram. Although this operation reduced the amount of data, the statistical inaccuracy associated with *Autoscala hm*F2 estimations, which is particularly high (up to 34.1 km) under disturbed geomagnetic conditions [Scotto and Sabbagh, 2020], was consequently decreased. Such

more reliable *hm*F2 values were then compared to the medians computed using the autoscaled values in the 27 days preceding the 9 May, to detect variations of the F2-layer height during the storm.

3.2 GNSS

We leverage ground-based GNSS receivers of a two-fold nature: (i) geodetic GNSS receivers for the evaluation of the Total Electron Content (TEC) and the Rate of TEC change Index (ROTI) [Pi et al., 1997]; (ii) Ionospheric Scintillation Monitor Receivers (ISMRs) able to provide the amplitude (S4) and phase (σ_ϕ) scintillation indices [Fremouw et al., 1978; Yeh and Liu, 1982]. The two receiver types and the associated datasets are described hereafter.

We make use of the GNSS scintillation data available in the eSWua database [Upper Atmosphere Physics and Radiopropagation Working Group et al., 2020c] covering the Mediterranean sector (green stars in Fig. 3). Specifically, we focus on data from three ISMRs Septentrio PolaRx5S [Bougard et al., 2011] equipped with choke-ring antennas, located in the Mediterranean region. One is located on the Lampedusa Island (id: *lam0p*, 35.52°N, 12.63°E), Italy, hosted at the Climate Observation Station of the Italian National Agency for New Technologies, Energy, and Sustainable Economic Development (ENEA); one at the Pizzi Deneri Volcanological Observatory, Catania, Italy (id: *cat0p*, 15.02°N, 37.77°E); one in Greece (id: *cha0p*, 35.52°N, 24.04°E), hosted at the Hellenic Mediterranean University of Crete. ISMRs like the PolaRx5s are multi-frequency multi-constellation receivers featured by a firmware able to provide, in quasi-real time, the widely adopted 1-minute S4 and σ_ϕ scintillation indices for each satellite-receiver pair. Enhancements of S4 values reveal the scintillation due to the presence of small-scale ionospheric irregularities from the GNSS perspective. These have a typical scale size below the Fresnel's scale for L-band signals and GNSS observational geometry from ground, i.e., a few hundreds of metres scale [Wernik et al., 2003]. As with the ISMRs we are interested in highlighting the spill-over of small-scale irregularities embedded in Equatorial Plasma Bubbles (EPBs) from low latitudes, triggered by the Mother's Day storm occurrence, we concentrate on S4 values from GPS, Galileo, Beidou and Glonass satellites. This is not the case of the receiver in Pizzi Deneri Volcanological Observatory (*cat0p*), characterised by a noisy multipath environment which masks the S4 enhancements due to ionospheric scintillation [see, e.g., Romano et al., 2013; D'Angelo et al., 2015; Li et al., 2022]. For that receiver, we make use of the σ_ϕ based on the standard phase detrending scheme made by a 6^{th} order Butterworth filter with a 0.1 Hz cutoff frequency [see, Ghobadi et al., 2020 and references therein], which is able to depict the phase fluctuations due to the presence of EPBs [Spogli et al., 2013].

We also leverage data in Receiver INdependent EXchange (RINEX) format with a 30 s time resolution from geodetic GNSS receivers to complete and extend the information provided by ISMRs. Specifically, we make use of the RING network (http://ring.gm.ingv.it/) [INGV RING working group, 2016], managed by the INGV. RING is a geodetic research infrastructure composed of a distributed network of over 200 GNSS sensors across Italy (orange circles in Fig. 3). Each station is equipped with a professional multi-frequency multi-constellation receiver and a choke ring antenna and, despite being conceived for crustal deformation monitoring and investigation purposes, its value for ionospheric studies has been already demonstrated [Cesaroni et al., 2017; Musico et al., 2018; Tornatore et al., 2021; Pignalberi et al., 2024a].

A subset of RING receivers has been selected for the application of the IONORING (IONOspheric RING) algorithm based on achieving a balance between homogeneous ionospheric coverage and minimal latency in product availability [Cesaroni et al., 2021]. Using the code and phase observables on L1 and L2 frequencies, IONORING evaluates TEC along each slant path connecting GNSS satellites and receivers to provide real-time maps of vertical TEC (vTEC) over Italy. Maps have a 10-minute time resolution and are in the latitudinal and longitudinal ranges of 35°N-48°N and 5°E-20°E, respectively. The IONORING vTEC maps are part of the data collections available in the eSWua data portal [Upper Atmosphere Physics And Radiopropagation Working Group, 2020d]. To better constrain the interpolation of the vTEC at the edges of the IONORING maps, further receivers from the EUREF network [Bruyninx et al., 2009] are dynamically added depending on their availability. A detailed description of the IONORING algorithm, including its validation, can be found in Cesaroni et al. [2021].

Besides leveraging on the vTEC information provided by the IONORING maps, we computed the ROTI [Pi et al., 1997] for each satellite-receiver pair with an elevation angle exceeding 20°, using 5-minute intervals and exploiting the RINEX data from RING and selected EUREF receivers, as indicated in Figure 3. Together with S4 index, ROTI can support the identification of the ionospheric scales involved in the observed fluctuations of the GNSS amplitude scintillation and phase observed at the ground. This is because S4 is affected by small-scale

irregularities, while ROTI enhancements due to the passage through EPBs are caused by irregularities with typical scales of several kilometres or more [Alfonsi et al., 2011, 2021; Yang and Liu, 2016; Spogli et al., 2023]. Both scales appear in cascades from larger to smaller during the growth and decay processes of EBPs.

3.3 Magnetometers

We use geomagnetic data recorded at three permanent observatories (blue squares in Fig. 3), which cover the entire latitudinal extent of Italy. From North to South, these observatories are Castello Tesino (geographic coordinate 46.05°N, 11.39°E), Duronia (geographic coordinate 41.65°N, 14.47°E), and Lampedusa (geographic coordinate 35.52°N, 12.55°E). At these observatories, regular automatic recordings of the horizontal component, declination, vertical component, and total intensity of the magnetic field are performed along with routine absolute measurements that facilitate the reconstruction of the baseline. Absolute measurements are performed using a theodolite and a proton magnetometer, which determine the true magnetic North and the baseline values for each component.

In addition to these permanent observatories, two temporary stations installed on the Etna volcano (Sicily), equipped with vector magnetometers, have provided valuable data, defining the extension and typology of the event under investigation. These temporary stations, located at Serra Pizzuta and Monte Crisimo, at geographic coordinates of 37.69°N, 15.03°E and 37.80°N, 15.10°E, respectively, enhance our ability to capture localised geomagnetic variations associated with volcanic activity.

The observatories' systems are designed to ensure high reliability and precision in measurements. Each observatory is equipped with two identical systems, each consisting of a fluxgate magnetometer and a scalar magnetometer. The fluxgate magnetometers measure the three orthogonal components of the geomagnetic field, providing vector data, while the scalar magnetometers measure the total magnetic field intensity. The combination of these instruments allows for comprehensive monitoring of the geomagnetic field's temporal and spatial variations. Regular calibration and maintenance of these instruments are conducted to preserve the accuracy of the recorded data.

Magnetic field vector components are recorded at a 1-second sampling rate and distributed as 1-minute averages. Definitive 1-minute cadence data can be retrieved at the INGV data portal (http://geomag.rm.ingv.it/) where, for each observatory, also the local K index can be downloaded. In this study, we used preliminary 1-minute data for the observatories of Castello Tesino, Duronia and Lampedusa and 1-second data for the station of Monte Crisimo and Serra Pizzuta. All these data do not include the baseline. These data provide a detailed temporal resolution, for the examination of rapid geomagnetic variations during Space Weather events.

3.4 Satellite data

To complete the information provided by the INGV network, we make use of satellite data.

The ESA's Swarm satellite mission [Friis-Christensen et al., 2008] consists of a constellation of three satellites named Alpha (A), Bravo (B), and Charlie (C), which operate in quasi-Sun-synchronous near-polar low-Earth orbits at different altitudes. Swarm A and C form the lower pair of satellites, flying in proximity throughout the mission, while Swarm B is in a higher orbit. During the Mother's Day storm, Swarm A and C were orbiting at approximately 480 km above the Earth's surface, while Swarm B was at a higher altitude of about 510 km. These satellites are equipped with various instruments to monitor the Earth's magnetic field and the ionosphere. One of these instruments is constituted by a pair of Langmuir Probes (LPs), which measure the plasma density and temperature in the ionosphere, investigated in this paper. Swarm LPs are included in the Electric Field Instrument (EFI) payload and provide observations at 2-Hz rate in harmonic mode [Knudsen et al., 2017; Catapano et al., 2022]. LPs data are provided as a Level 1b product in a common data format (CDF) through the public repository at https://swarm-diss.eo.esa.int/. Despite being conceived mainly as a magnetic mission, Swarm proved to be valuable for insights on the ionospheric plasma dynamics and morphology [see, e.g., the thorough review by Wood et al., 2022].

We also leverage the thermospheric information obtained from the Global UltraViolet Imager (GUVI) on NASA's Thermosphere, Ionosphere, and Mesosphere Energetics and Dynamics (TIMED) satellite [Christensen et al., 2003]. The TIMED/GUVI instrument provides measurements of the column-integrated [O]/[N_2] ratio, where [O] represents the numerical density of atomic oxygen and [N_2] represents the density of molecular nitrogen. The primary

production process for F-region O^+ plasma is the photoionization of atomic oxygen, while the main loss process for O^+ involves reactions with molecular species such as N_2 and O_2. Consequently, the density of O^+ tends to vary with the $[O]/[N_2]$ ratio. Thus, the $[O]/[N_2]$ data can offer insights into how thermospheric composition affects the variability of ionospheric plasma density during storms.

3.5 Vertical TEC, bottom vertical TEC, top vertical TEC and slab thickness

The ionospheric response is also investigated by analysing vTEC, topside vTEC (hereafter tTEC) and bottomside vTEC (hereafter bTEC).

The vTEC values are provided by the IONORING real-time maps, whereas bTEC values were obtained through the International Reference Ionosphere UPdate (IRI UP) data-assimilation method. IRI UP is a nowcasting version of the International Reference Ionosphere model (IRI) [Bilitza et al., 2022] aiming at improving the description of the ionospheric F2-layer peak through the calculation of ionospheric effective indices and following ingestion in IRI. IRI UP, initially based only on the assimilation of ionosonde data [Pignalberi et al., 2018], was then updated to allow assimilating vTEC data from ground-based GNSS receivers [Pignalberi et al., 2019]. In addition, Pignalberi et al. [2024a] have recently proposed a tailored version of the IRI UP method based on the assimilation of real-time vTEC maps by IONORING to generate real-time F2-layer ordinary critical frequency (*fo*F2) maps over Italy. Since the F2-layer peak is an anchor point in the IRI model formulation, the update of *fo*F2 modifies the entire vertical electron density profile shape. Therefore, real-time values of *fo*F2 provided by IRI UP provide an update of the bottomside vertical electron density profile which is numerically integrated to obtain an estimation of the bTEC. The tTEC is then obtained as the difference between vTEC and bTEC.

Values of vTEC, tTEC and bTEC were calculated every 10 minutes from 9 May at 12:00 UT to 14 May at 23:50 UT. The ratio bTEC/vTEC has been recently proven as a meaningful tool revealing the role of vertical plasma transport in the ionosphere and on the plasmasphere/ionosphere relative balance during a storm [Pezzopane et al., 2019].

Moreover, for the same period the ionospheric equivalent slab thickness (τ), defined as the ratio of vTEC to *Nm*F2, was calculated at the same time resolution. τ is an important parameter to characterise the shape of the vertical electron density profile and, consequently, the plasma distribution in the extremely dynamical system composed by the ionosphere and plasmasphere [Pignalberi et al., 2021, 2022, 2024b]. For this study, we calculated real-time τ values as the ratio between vTEC from IONORING and *Nm*F2 from IRI UP. Moreover, for comparison, the τ climatological behaviour has been derived by using a long time series of observations from co-located ionosonde and GNSS receiver at the Rome ionospheric station, as detailed in Pignalberi et al., [2022].

4. Results and discussion

An overall picture of the geomagnetic response over Italy for the event under investigation is displayed in Figure 4. The figure shows, from top to bottom, the local K index estimated from measurements at Duronia observatory [Regi et al., 2020] (Fig. 4a), the variation ΔH of the horizontal component as measured at the observatories of Castello Tesino in Northern Italy (Fig. 4b), Duronia in Central Italy (Fig. 4c), Lampedusa in Southern Italy (Fig. 4d) and at the magnetic station of Monte Crisimo on Etna volcano (Fig. 4e). Due to the proximity, Serra Pizzuta observatory does not show any meaningful differences relative to Monte Crisimo. Therefore, it is not discussed any further. We recall that plotted data are just variations, i.e., they are not adjusted for baseline changes and, to better compare them, we subtracted from each time series its value at 17:05 UT.

As well displayed by the local K index, geomagnetic activity reached very high values at mid latitudes and, apart from slight differences, it agrees with the behaviour of the global Kp index. The variation ΔH at the three observatories show a clear SSC characterised by a rise-time of 3 minutes and by an amplitude of 139 nT at Castello Tesino, 124 nT at Duronia and 100 nT at Lampedusa. These values display a decrease of SSC with decreasing latitude. The SSC we observe in Figure 4e, at Monte Crisimo is instead of 183 nT. The fact that this value is so high compared to other observatories, despite its latitude, is due to the use of 1-second measurements at this station instead of 1-minute averages. Indeed, by averaging these data over 1 minute we obtain a value for the SSC between that of Lampedusa and Duronia. Nevertheless, the use of 1-second data evidences the fine scale of geomagnetic field time variations. This is very important, for instance, in the investigation of Space Weather hazards as the buildup of

geomagnetically induced currents (GIC). After the SSC, at all the observatories, the variation ΔH continues to grow reaching, in a time interval of around half-an-hour (at 17:40 UT on 10 May), 238 nT at Castello Tesino, 209 nT at Duronia, 167 nT at Lampedusa and 255 nT at Monte Crisimo. If we consider the minimum value reached by ΔH at around 10 UT on 11 May, the overall variation in Italy has been of the order of 600 nT. This is one the highest values recorded in the last 30 years, topped only by the Halloween storm that occurred in October 2003, when the maximum variation exceeded 700 nT.

A detailed investigation of the variations recorded by magnetometers shown in Figure 4 reveals the modulation due to the IMF Bz component and SW speed and density. For instance, as described in Section 2, we know that on 10 May 2024 at 16:40 UT DSCOVR showed that speed abruptly jumped from 450 to 700 km/s and density from 5 cm^{-3}

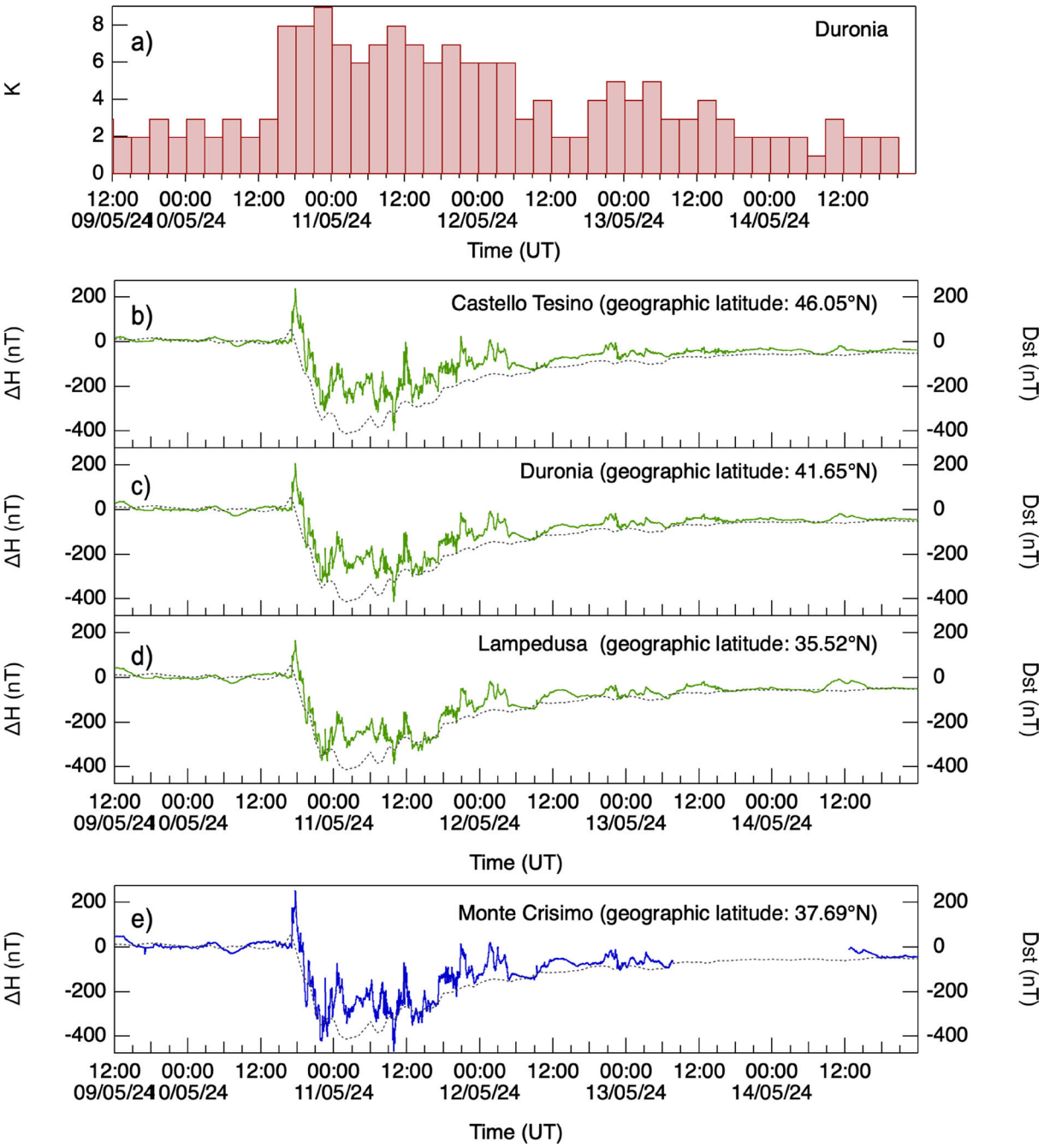

Figure 4. Local K index for Duronia observatory (panel a), variation ΔH of the horizontal component of the geomagnetic field recorded at the observatories of Castello Tesino (panel b), Duronia (panel c), Lampedusa (panel d) and at the station of Monte Crisimo (panel e). In panels b), c), d) and e), Dst index (dotted grey line) is plotted for reference. Data cover the period from 9 May 2024 12:00 UT to 14 May 2024 23:59 UT.

to 40 cm^{-3}. The delay time of 25 minutes between the recording of the CME by DSCOVR at L1 and the occurrence of the SSC is well in agreement with the SW speed displayed in Figure 2. Time variations following the SSC are clearly dependent on the combined effect of the variations in IMF Bz and SW speed and density. Enhancement of the ring current, and hence the decrease in the variation ΔH of the horizontal component, is facilitated by negative Bz and high values of speed and density. On the other hand, enhancements of the magnetopause currents are possible also under conditions of positive Bz and abrupt increases in speed and density. This could be the reason for increases in ΔH at ground observatories that are visible starting from around 18 UT on 12 May: e.g., at around midnight of 11 May and between 12 and 13 of May. At these times, Bz is mostly positive, but some abrupt changes can be identified in the speed and density (Fig. 2). The variation, present in all observatories but particularly visible at Lampedusa at 12 UT of 12, 13 and 14 of May has, instead, nothing to do with the geomagnetic storm, being a signature of the solar quiet daily variation.

Figure 5 shows the IONORING vTEC maps generated at 12:00 UT from 9 to 14 May from which a plasma decrease following the beginning of the storm is clear on both 11 and 13 May. Another significant feature coming out from the figure is the counterclockwise rotation of the vTEC gradient characterising both the 12 and the 13 May, which demonstrates the unusual and disturbed ionospheric conditions. Figure 6a shows instead, from 9 May at 12:00 UT to 14 May at 23:50 UT, the time series of both the mean vTEC and the corresponding standard deviation, calculated from IONORING maps, as those shown in Figure 5, routinely generated every 10 minutes, along with the corresponding 27-day median values calculated before the 9 May. Figure 6a shows also the daily mean of the $[O]/[N_2]$ ratio as obtained from GUVI measurements taken over the same region covered by IONORING. Figure 6b reports the vTEC deviation with respect to the corresponding 27-day median values, as a function of time and latitude. Figure 6 as a whole clearly highlights how the significant plasma depletions characterising the 11 and 13 May are strictly connected to an important decrease of the $[O]/[N_2]$ ratio, which is mostly at the base of a significant decrease of the *fo*F2 and of the vTEC. Figure 6b highlights also that the vTEC depletion recorded at the beginning of the storm is caused by an equatorward meridional thermospheric wind moving from the auroral zone toward mid latitudes. Indeed, the vTEC depletion starts at 48°N on 10 May at about 18 UT and reaches the lowest part of the IONORING region, corresponding to 36°N, only a few hours later.

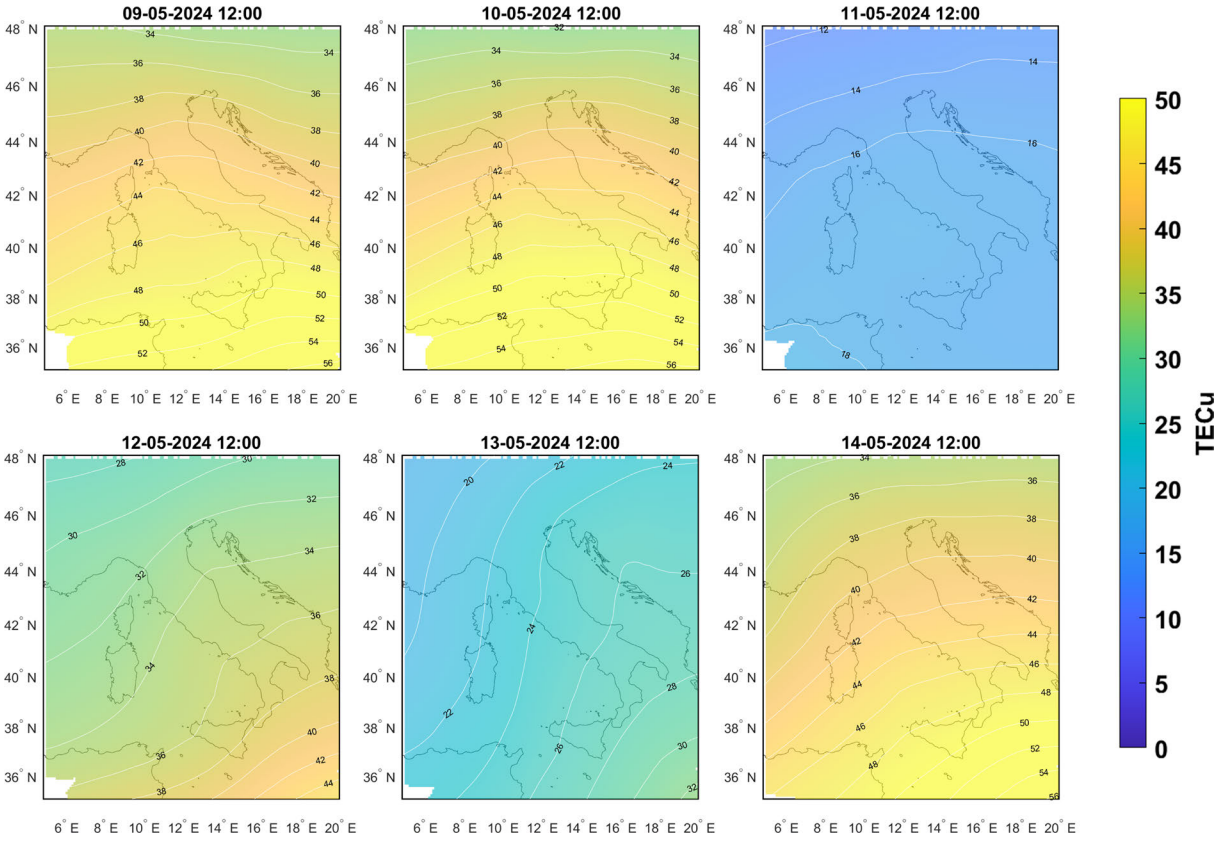

Figure 5. IONORING vTEC maps at 12:00 UT from 9 to 14 May 2024.

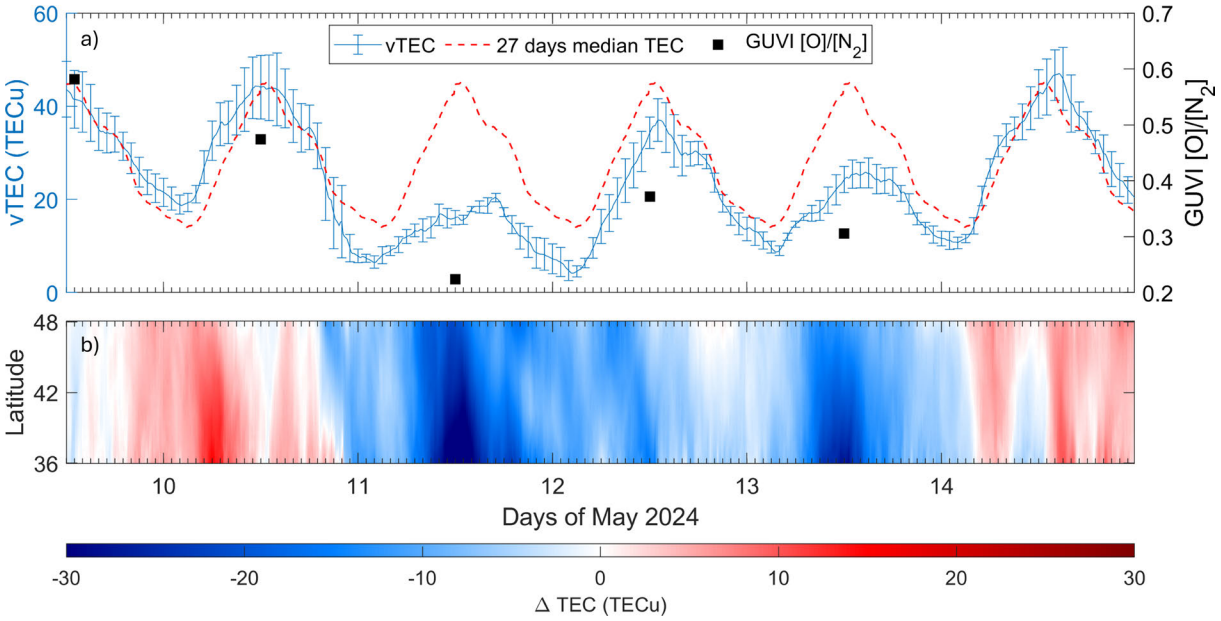

Figure 6. Panel a) shows from 9 May 2024 at 12:00 UT to 14 May 2024 at 23:50 UT the time series of mean and standard deviation of vTEC over the region covered by IONORING maps (blue curve), the corresponding 27 days median values as quiet reference (red dashed curve) and the daily mean of the $[O]/[N_2]$ ratio as obtained from GUVI measurements over the same region (black squares). Panel b) reports the deviation of the vTEC with respect to the corresponding 27 days median values as a function of time and latitude.

Figures 7 and 8, from 9 May at 12:00 UT to 14 May at 23:50 UT, show respectively for Rome and Gibilmanna the trends of: *fo*F2 as obtained from IRI UP according to Pignalberi et al. [2024a]; *fo*F2 as output by the IRI-2020 model; manually scaled *fo*F2 values as measured by the AIS-INGV ionosonde and the corresponding 27-day median calculated before the 9 May; *hm*F2 as validated from the autoscaling made by *Autoscala* and the corresponding 27-day median calculated before the 9 May; bTEC, tTEC and vTEC and the corresponding ratio tTEC/bTEC; the real-time slab thickness based on IRI UP values and the climatological one. Concerning the 11 May, it is worth noting that *fo*F2 and *hm*F2 are often characterised by a lack of data, that is because a number of solar flares occurred during the period of the storm. In these instances, the intense D-region absorption resulting from increased ionisation due to X-ray emissions hindered the observation of ionogram traces. Moreover, a number of ionograms are characterised either by spread-F or by a height of the trace of the F region exceeding the range sounded by the ionosonde; it is also worth noting that a limited number of ionograms are characterised either by a G condition, namely a condition for which *fo*F2 is equal or lower than the critical frequency (*fo*F1) of the F1 layer [e.g. Deminov et al., 2011], or by a blanketing sporadic E layer. *fo*F2 values manually-scaled from ionograms provide a reference for the evaluation of the IRI UP IONORING data-assimilation model ability to nowcast *fo*F2 short-term and small-scale variations. Figures 7a and 8a confirm the IRI UP IONORING reliability for both quiet and severely disturbed conditions, as already evidenced by Pignalberi et al. [2024a]. However, it is worth highlighting how IRI UP IONORING shows an overestimation of *fo*F2 during the main phase of the storm in the evening between 10 and 11 May, while the agreement with ionosonde observations is remarkable during the recovery phase. This discrepancy might be due to the combination of the following issues: 1) during the main phase of the storm the correspondence between vTEC and *fo*F2, which is assumed by IRI UP IONORING, is reduced, and the assimilation of vTEC values does not fully describe *fo*F2 variations; 2) *fo*F2 strongly decreases during the main phase of the storm but this is associated with a simultaneous abnormal increase of *hm*F2. The combination of the two slightly mitigates the vTEC decrease, which in turn results in an overestimation of *fo*F2 by IRI UP IONORING. This explanation is supported by the fact that *fo*F2 modelled values during the recovery phase, where *hm*F2 exhibits a behaviour much more in line with the median one compared to the main phase, are in better agreement with observations. Since IRI UP IONORING is based on the assimilation of an integrated quantity like vTEC, such abnormal variations in the altitude of the F2-layer peak and in the shape of the vertical electron density profile characterising the main phase of the storm are hardly captured by the model.

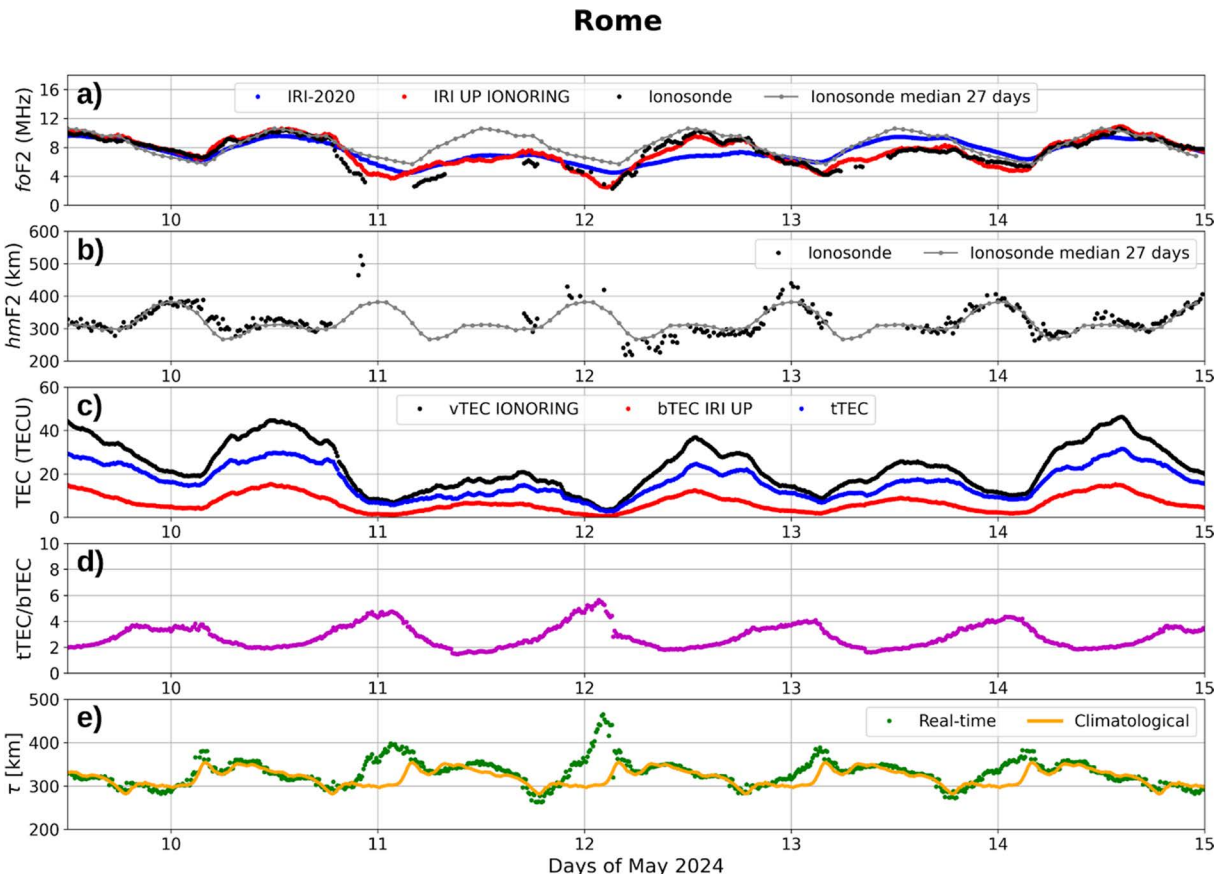

Figure 7. Time series of several measured and modelled ionospheric parameters at the Rome ionospheric station from 9 May 2024 at 12:00 UT to 14 May 2024 at 23:50 UT. Panel a) shows *fo*F2 values from manually-scaled ionograms (black points), 27-day *fo*F2 medians for the reference quiet period before the 9 May (grey points connected by solid line), *fo*F2 modelled by IRI-2020 (blue points), and *fo*F2 modelled by IRI UP IONORING (red points). Panel b) shows *hm*F2 values measured by ionosonde (black points), and 27-day *hm*F2 hourly medians for the reference quiet period before the 9 May (grey points connected by solid line). Panel c) shows vTEC values modelled by IONORING (black points), bTEC modelled by IRI UP (red points), and tTEC as the difference between vTEC and bTEC (blue points). Panel d) shows the time series of the ratio tTEC/bTEC (magenta points). Panel e) shows τ values as obtained by combining the outputs of real-time IONORING and IRI UP models (green points), while the orange solid line shows the climatological diurnal behaviour of τ at the Rome station, for the seasonal and solar activity conditions according to Pignalberi et al. [2022].

Figures 7 and 8 confirm what was already highlighted by Figures 5 and 6, that is the significant depletion characterising the ionospheric plasma occurring on 11 and 13 May, which is here well visible also in *fo*F2. Negative phases like these are thought to be caused by neutral composition changes [e.g. Buonsanto, 1999; Mendillo, 2006]; specifically, by a decrease of the $[O]/[N_2]$ ratio, which triggers a strong reinforcement of the ion loss rate [Prölss, 1995]. Indeed, the energy dissipated by the solar wind causes an increase of the exospheric temperature which affects the density structure of the polar upper atmosphere. This triggers an increase of the heavier gases (especially the molecular nitrogen N_2) and probably the storm thermospheric circulation determined a decrease of the atomic oxygen O. Anomalous disturbed composition is a usual feature at high latitudes, but during more active conditions, as the ones recorded during this extreme Space Weather event, this disturbed composition moved from auroral toward lower latitudes, as well highlighted by Figure 6. On 12 May the ionospheric trends seemed to recover to pre-storm conditions, but on 13 May a new negative phase was still well visible. Regarding this, we speculate that on 12 May the uplift of the F2 layer, contrary to what happens on 11 May, succeeds in counterbalancing the plasma decrease caused by neutral composition changes that are less intense than on 11 May. The F2-layer uplift is evident in the ionogram series (not shown) and perceivable in *hm*F2 values reported in Figures 7b and 8b. During the night between 12 and 13 May a new increase of geomagnetic activity, less intense than that which occurred on 10 May, was

observed and followed by a new negative ionospheric phase. This new increase of geomagnetic activity, as testified by the increase of the IMAGE electrojet indicators, might be ascribed to an additional energy dissipation in the polar areas, most likely related to both the Southward inversion of the IMF Bz component which lasted for a few hours at the end of 12 May and to the sudden variations of the SW pressure. According to Prölss [1995], the aforementioned uplift can be attributed to both travelling atmospheric disturbances (TADs) and large-scale changes in the wind circulation, both of them triggered by the significant amount of energy injected into the polar atmosphere. Of course, for both 11 and 13 May an outflow of plasma from the ionosphere to the overlying plasmasphere might have played a significant role [Pezzopane et al., 2019].

Figures 7 and 8 show that for both Rome and Gibilmanna tTEC and bTEC variations are similar to that of vTEC, while the corresponding ratio tTEC/bTEC shows a significant increase at Gibilmanna between 10 and 11 May and between 11 and 12 May, which is only slightly evident at Rome. At both sites the bTEC values are similar, and very low, which suggests that the lower part of the vertical electron density profile is dominated by neutral composition changes. What changes is the tTEC, which is higher at Gibilmanna than in Rome. This could have been caused by an intensification of nighttime poleward thermospheric meridional winds, whose effect is more pronounced in Gibilmanna than in Rome [Titheridge, 1995]. The ionospheric impact is also apparent on slab thickness time series shown in Figs. 7e and 8e. The comparison between real-time and climatological values highlights that, at both stations, the nighttime τ values are enhanced well-above the expected climatological values during the main phase of the storm and in the following days of the recovery phase. In particular, the highest enhancements have been recorded at the beginning of 12 May, particularly at Rome station, with values up to 450 km. On the other hand, daytime real-time τ values slightly differ from the climatological reference, irrespective of the geomagnetic conditions. The lowest τ values have been recorded at dusk hours on 11 May, particularly at Gibilmanna station, where values just above 250 km have been recorded. Since τ is a proxy of the ionosphere plasma scale height at the F2-layer peak [Wright, 1960; Hibberd and Ross, 1966], it provides information on the electron density profile shape around the F2-layer peak [Pignalberi et al., 2022, 2024b]. In particular, the exceptionally high τ values during nighttime point out a thickening of the F2-layer profile shape, which is induced by a remarkable vertical transport of

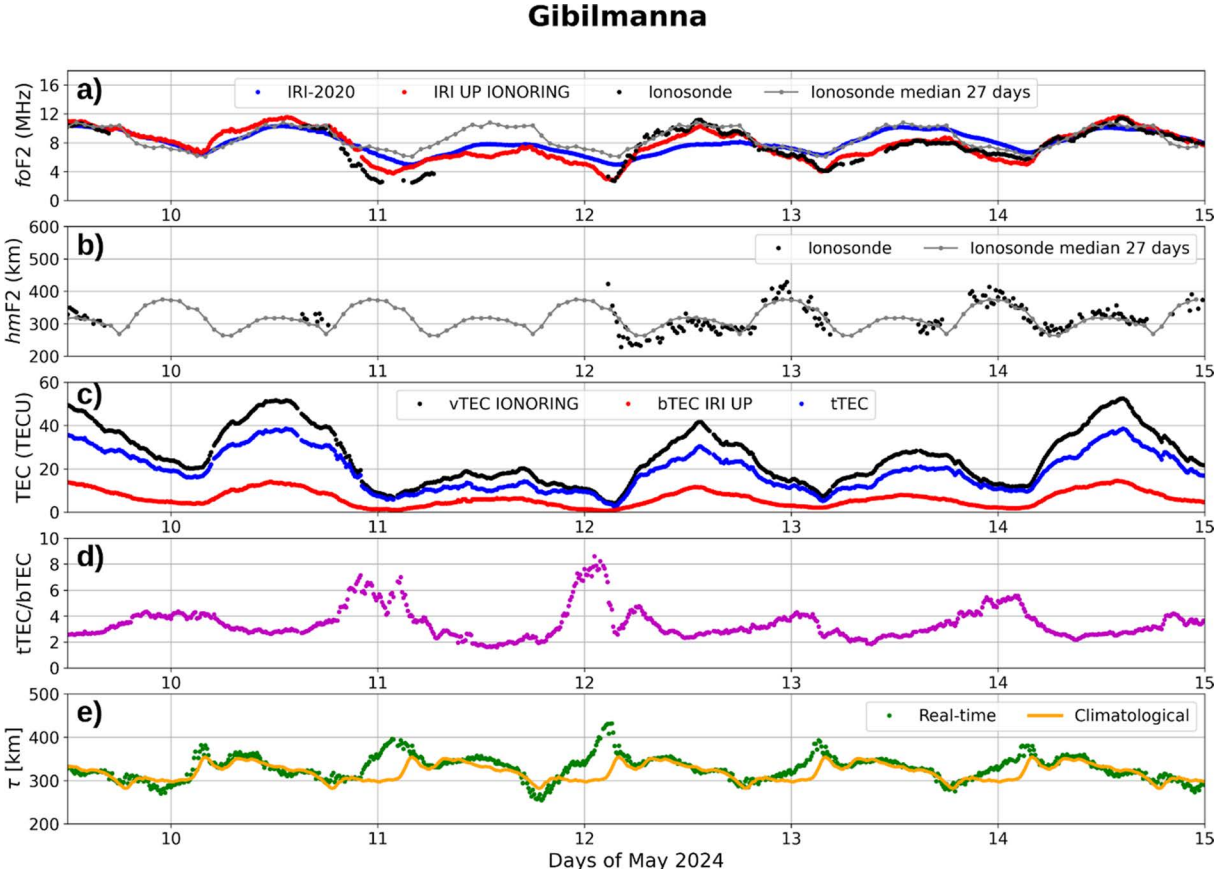

Figure 8. Same as Figure 7 but for the Gibilmanna ionospheric station.

plasma (uplift) from the bottomside to the topside ionosphere. This agrees with the variation of the ratio tTEC/bTEC, which also maximises at nighttime. This hypothesis is supported by the *hm*F2 time series obtained from ionosonde measurements. It is worth noting that between 10 and 11 May, during the main phase of the storm, *hm*F2 remarkably increased over the median quiet reference; a similar behaviour, albeit smaller in magnitude, is also visible for the next two nights of the recovery phase. These observations highlight how during nighttime and under disturbed conditions the ionosphere is affected by a remarkable uplift of plasma which raises the altitude of the F2 layer and, at the same time, stretches the profile in an abnormal way, compared to quiet conditions.

We also investigate the occurrence of small- and medium-scale irregularities from the GNSS perspective by integrating the S4 and ROTI information provided by the ISMRs, and the RING and selected EUREF geodetic receivers, respectively.

We make use of the Equatorial Electric Field (EEF) model from Cooperative Institute for Research in Environmental Sciences (CIRES) of the University of Boulder, Colorado. The model is based on a correlation analysis between the Interplanetary Electric Field (IEF) parameters provided by DSCOVR and the EEF and it can highlight the role of the Prompt Penetrating Electric Fields (PPEFs) [Wei et al., 2015] in the EEF budget, to speculate on the EPB occurrence. Specifically, the model uses a transfer function model to predict the EEF variation from IEF data and a climatological model to account for the quiet day variations of EEF [Manoj et al., 2008, 2013; Manoj and Maus, 2012]. The output of the model in the considered longitudinal sector (around 13°E) is shown in Figure 9a. Specifically, it shows the quiet EEF (blue), the EEF with the contribution of PPEFs (green) and the contribution ΔEEF due to PPEFs (red). The purple dashed lines indicate the time of the sunset at the magnetic equator.

Figures 9b-d show the time profiles of S4 from Lampedusa (b) and from Chania (c) and of σ_ϕ for Pizzi Deneri Volcanological Observatory, Catania (d). Black circles refer to observations at elevation angles >5°, while red circles to angles >20°. Figure 9e shows time profiles of ROTI from the RING and selected EUREF stations. Colour code indicates the latitude of the IPPs at 350 km.

The night between 9 and 10 May, i.e., before the storm's arrival, is characterised by the presence of post sunset EPBs, as highlighted by the increase of S4 at both *lam0p* and *cha0p*, mostly at low elevations. The ROTI and σ_ϕ

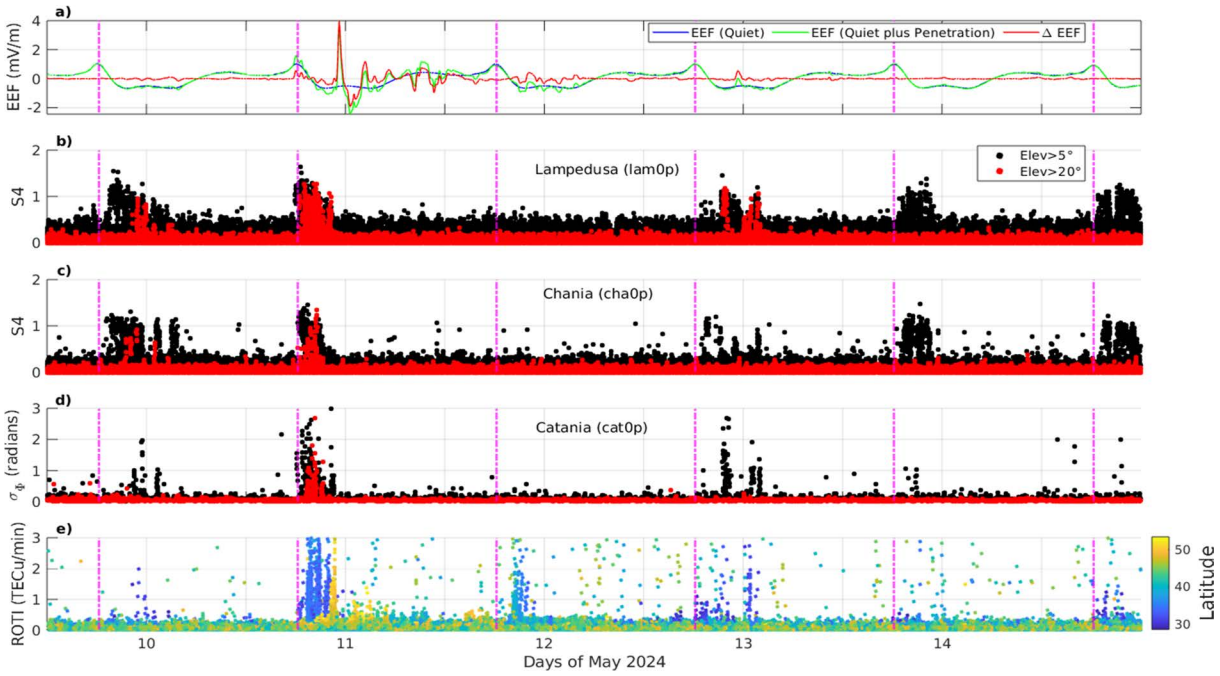

Figure 9. (Panel a) Time series of Quiet EEF (blue), EEF with contribution of PPEFs (green) and ΔEEF due to PPEFs (red). Time series of S4 from Lampedusa (panel b) and from Chania (panel c) and of σ_ϕ for Pizzi Deneri Volcanological Observatory, Catania (panel d). Black circles refer to observations at elevation angles >5°, while red circles to angles >20°. (Panel e) Time series of ROTI from the RING and selected EUREF stations. Colour code indicates the latitude of the IPPs. The purple dashed lines indicate the time of the sunset at the magnetic equator. Time range is from 12:00 UT on 9 May to 23:59 UT on 14 May.

measurements indicate that the EPB signature did not appear over the sector under investigation. This is an expected climatological feature related to EPB occurrence in the African sector [see, e.g., Yizengaw & Groves, 2018].

During the night between 10 and 11 May, the arrival of the storm causes the undershielding conditions modifying the Region 1 and Region 2 Field-Aligned Currents and triggers PPEFs at the time of the local sunset at the magnetic equator in the considered longitudinal sector. This is evidenced by the increase of ΔEEF (red curve in Fig. 9a) in correspondence with the EEF Pre-Reversal Enhancement (PRE) at sunset. This causes a stronger **E**x**B** drift at the magnetic equator, a consequent larger uplift of the F region, and this mechanism results into EPBs entering in the field of view of the GNSS receivers, as proved by increases of S4 at higher elevation angles (red dots in Figs. 9b-d) and ROTI (at lower latitudes, bluish dots in Fig. 9e). It is worth recalling that, even a small PPEF-like effect on the EEF can cause a meaningful poleward displacement of the EPBs signature [Alfonsi et al., 2021].

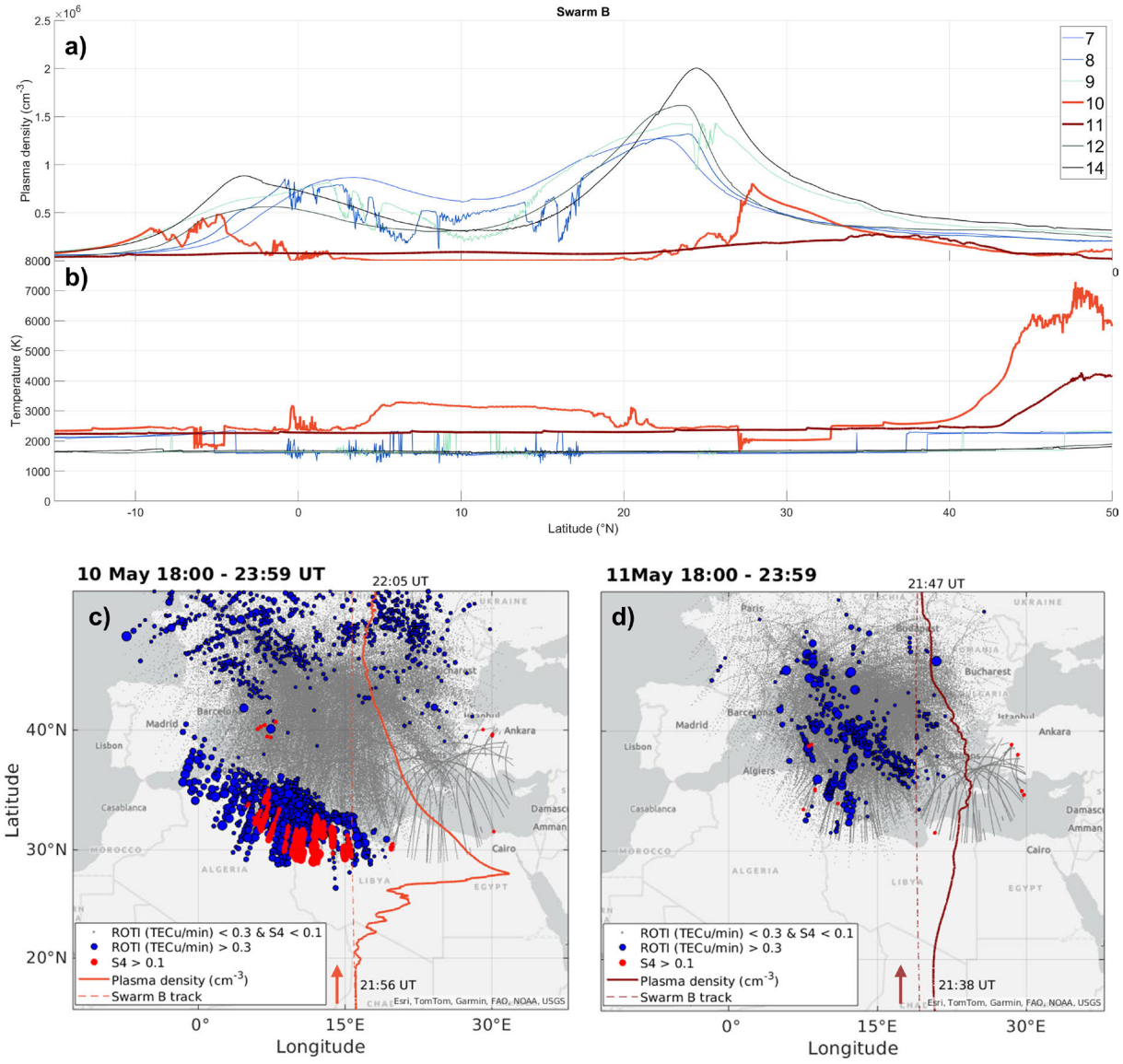

Figure 10. Latitudinal profiles of the plasma density (panel a) and temperature (panel b) measured by Swarm B (nighttime tracks) in the longitudinal range of the IONORING maps (5°E-20°E) for the period 7-14 May. (Panel c) ROTI >0.3 TECu/min (blue dots), S4>0.1 (red dots) at an IPP of 510 km and for 10 May between 18:00 UT and 23:59 UT. Grey dots represent ROTI and S4 values below the aforementioned threshold. The light red dashed line represents the ground track projection of the passage between 21:56 UT and 22:05 UT on 10 May. The light red thick line indicates the in-situ plasma density of Swarm B with a higher longitudinal positive deviation from the ground track, the higher the plasma density is. The red arrow indicates the direction of the satellite. (Panel d) Same as panel c but for 11 May, the IPPs are at 350 km and the dark red information refers to Swarm B between 21:38 UT and 21:47 UT.

A feature worth noticing is just around 00:00 UT on 11 May: strong positive and negative PPEFs events occur in correspondence with ROTI increases at higher latitudes (yellowish dots in Fig. 9e). Another striking feature is the increase of ROTI (with no related S4 and σ_ϕ events) in the post sunset hours of the night between 11 and 12 May. Those two storm-triggered events deserve a more detailed description, as provided in Figure 10 and related text. We must stress that Figures 9b-e show that on 14 May scintillation (and ROTI) activity started going back to the pre-storm conditions, with scintillation and phase fluctuation events mostly involving low elevation satellites in the Southernmost part of the field of view of the GNSS receivers.

As mentioned above, we focused on the post-sunset hours of 10 and 11 May and we complement the GNSS-based information with that provided by the Swarm B satellite, that covered the local time sector at about 23 LT with its ascending tracks during the storm occurrence. Figures 10a and 10b show respectively the latitudinal profiles of the plasma density and temperature measured by Swarm B (nighttime tracks) in the longitudinal range of the IONORING maps (5°E-20°E) for the period 7-14 May. Figure 10c shows instead the ROTI > 0.3 TECu/min (blue dots) and S4 > 0.1 (red dots) on 10 May between 18:00 UT and 23:59 UT. Grey dots represent ROTI and S4 values below the aforementioned thresholds. In Figure 10c, the light red dashed line represents the ground track projection of the Swarm B passage between 21:56 UT and 22:05 UT on 10 May, while the light red thick line indicates the in-situ plasma density of Swarm B: the larger the longitudinal positive deviation from the ground track, the higher the plasma density. The red arrow indicates the direction of the satellite. Figure 10d reports analogous information to Figure 10c, but for 11 May, and the dark red information refers to Swarm B between 21:38 UT and 21:47 UT. Bearing in mind that when dealing with EPBs, the single irregularity layer approximation is not valid, the IPPs are set at 510 km for 10 May (Fig. 10c) to match the *hm*F2 reported in Figure 7b, which also enables a direct comparison with variations at Swarm B altitudes. For 11 May (Fig. 10d), we applied the same criterion, and we adopted a height of the IPP at 350 km.

Figure 10a clearly shows how the plasma density during the night of 10 and 11 May varies meaningful differently from the days before and after, as featured by the presence or absence of EPBs signatures, and, being in a latitudinal range which covers the low latitude sector of the Southern Hemisphere, shows the typical signature of the plasma peaks at the crests of the Equatorial Ionisation Anomaly (EIA). The plasma density on 10 May is very low (below 10^4 cm^{-3} around the equator), and its temperature is very high, when compared with the climatological picture provided by Pignalberi et al. [2024c]. Thus, on 10 May Swarm B is passing through a huge region of plasma depletion at high temperature, from about 0°N to 20°N, with signatures typical of EPBs only between 20°N to 28°N, i.e., Northern than in other days. This means that the plasma maps to higher flux tubes due to an enhanced **E**x**B** vertical drift caused by PPEFs. The very low background plasma density around the magnetic equator suggests that Swarm B is flying below the F region as visible from the ionograms registered by Gibilmanna AIS (not shown). In correspondence of the latitudinal range 20°N to 28°N, GNSS data presents enhancements in both ROTI and S4 (South-westernmost part of Fig. 10c). The partial superposition of S4 and ROTI enhancements provides further evidence of the different information provided by the two GNSS-related measurements. In fact, as already pointed out by Spogli et al. [2023], ROTI enhancements from 30-s data used at low latitudes are due to irregularities with a typical scale size of a few kilometres, being an intermediate scale in the plasma cascading towards the smaller scales (below hundreds of metres), which are conversely revealed by 1-minute S4 values. The orientation of these ROTI and S4 enhancements follow the magnetic equator orientation and can partly also relate to the fact that the westernmost African region was characterised by stronger PPEF events at sunset. This has been verified by using the same EEF model we used to produce Fig. 9a, but for the West Africa longitudinal sector (not shown).

For what concerns the ROTI enhancements in the northernmost part of the map (40°N-50°N) on 10 May, they are associated with small fluctuations in the Swarm B plasma density and, most notably, with an impressive increase of about 350% of the plasma temperature (~7300 K peak value) with respect to the climatological values reported in Figure S2 of Pignalberi et al. [2024c]. Such a feature may suggest that those ROTI enhancements can be ascribed to the presence of Stable Auroral Red (SAR) arcs. SAR arcs are related to the dynamics of the plasmasphere and ring current during storm times. A thorough description of SAR arcs and their different origin and evolution with respect to the strict polar aurora can be found in a recent review by Gallardo-Lacourt et al. [2021]. A scheme of the development of SAR arcs can be seen in Kozyra et al. [1987]. They are related to the combined effects of the equatorward motion of the plasmapause during geomagnetically disturbed periods and the heating of the cold plasma contained in the plasmasphere by the effect of the increased ring current intensity. Electrons in the plasmasphere are heated either by conduction or precipitation of particles from the ring current region, and when the electron temperature exceeds about 3000 K, the atomic oxygen is excited by collisions with ambient electrons,

giving rise to a spectrally pure red-light emission (630 nm photons). This should happen at the footprint of the overlapped plasmasphere and ring current regions, where two conjugate red arcs form (Northward and Southward of the equator), rather narrow in the North-South direction (50-200 km) but pretty much elongated in the East-West direction (thousands of km). Such combination of ROTI and electron temperature enhancements, along with the observations of red glows in the night sky all above Southern Europe (see Section 5 for more details) could therefore suggest that the plasmapause footprint has been shifted as far South as about 45° during the main phase of the storm.

Another possible contribution to the ROTI enhancement can be related to the presence of the ionospheric main trough that, under the strongest intensification of the auroral electrojet during that night (as in Fig. 2f), may have reached about 45°N in the European sector, as already happened during the 2015 St. Patrick Day's storm [Cherniak et. al., 2015]. In that case, the ROTI was found to vary between 0.1 and 0.5 TECu/min, similarly to our reported case. The location of the boundary of the auroral oval estimated through the Field-Aligned Currents product from Swarm [Lühr et al., 2015] (not shown) also confirmed that the equatorward boundary reached about 45°N-50°N.

For what concerns 11 May between 18:00 UT and 23:59 UT (Fig. 10d), no small-scale irregularities are detected, as testified by the very low values of the S4 index. On the other hand, ROTI enhancements feature two close geographical sectors: one over Tunisia and one forming a diagonal band in the latitudinal range 35°N-45°N and oriented in the NW-SE direction. The corresponding Swarm B information suggests the presence of a blob of low-density plasma in the range 20°N-45°N, with a peak plasma temperature of about 4000 K. Mid-latitude plasma blobs are notable mesoscale ionospheric structures, with many unknowns about the physical mechanisms ruling their formation. Kil et al. [2019] suggests that they are formed in association with either EPBs or Medium-Scale Travelling Ionospheric Disturbances (MSTIDs). According to Park et al. [2022], blobs are associated with the dynamics of EPBs, but simulations indicated that meridional winds could alter the plasma density distribution within an EPB flux tube, resulting in the formation of a plasma density enhancement (blob) at one end of the flux tube. Cesaroni et al. [2017] reported a signature similar to the one identified in Figure 10d, in the same region and with the same orientation, triggered by the 13-15 November 2012 geomagnetic storm, and due to convergence between a Large Scale Travelling Ionospheric Disturbance (LSTID) and the poleward expansion of the Northern crest of the EIA during nighttime. We believe that a similar mechanism could have occurred in the night under investigation. Specifically, the ROTI over Tunisia (around 32°N, 14°E) and the Southernmost part of the Swarm B plasma measurements suggests the presence of EPB-embedded-like medium scale irregularities.

This may indicate that a F-region uplift at the magnetic equator may have taken place. However, the bottomside gradient did not initiate the Rayleigh-Taylor instability and the EPB was not completely able to decay towards small-scale irregularities. What we miss in this picture is the possible role of the Disturbance Dynamo Electric Fields (DDEFs), which may have played a role in the aforementioned mechanism. In conclusion, the plasma density fluctuations featuring the blob suggest the presence of LSTID-like wavelike structures, suggesting that the blob is again generated, like in Cesaroni et al. [2017], by the convergence of plasma of low-latitude origin triggered by the PRE and acting in the post-sunset hours (at the local magnetic equator) and wave-like perturbations that were identified propagating equatorward.

5. Event communication to the public

In the context of communication activities, a significant contribution is made by the "Space Weather Monitoring Group" (SWMG), operating within the INGV Environment Department. The group's initiatives address various communication channels, including the communication of Space Weather events to the public through social media, the publication of short articles in the Environment Department blog termed "INGVambiente" (https://ingvambiente.com/ available exclusively in Italian at present), and the issuance of weekly bulletin of Space Weather for the Mediterranean Area aimed at specialised audience. Subsequent sections detail the group's communication efforts during both the Mother's Day storm.

5.1 Communication on Italian social media

The Mother's Day superstorm was preceded by intense solar activity, which the SWMG group reported almost daily on the social media channels of the INGV Environment Department. On the aforementioned "INGVAmbiente"

blog, a post anticipating an increase in solar activity was published at the end of April. Titled "Dancing Among the Stars: The Spectacle of Auroras", this publication proved particularly useful in the following days, when the Mother's Day storm manifested as a series of luminous events observed across the entire Italian peninsula. Approximately a week later, a second post titled "A Week of Ordinary Solar Madness!" was published, focusing on the observed solar activity within the context of the current phase of the solar cycle. The description of the activity was consistently present on the department's social media channels, varying in frequency and content according to the characteristics and interests of the audience of the different platforms, as detailed hereafter.

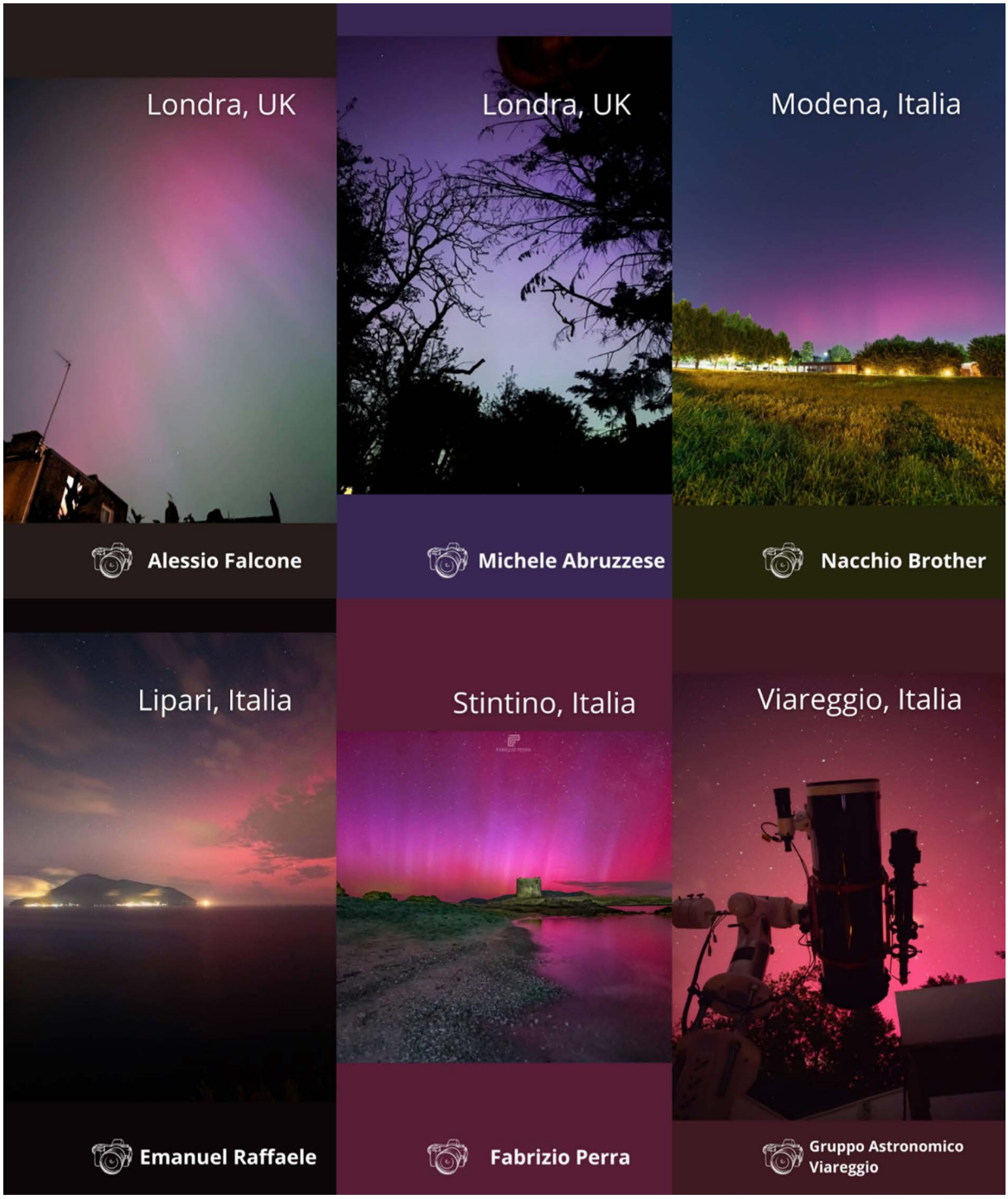

Figure 11. Some of the images from the highlighted stories on INGVambiente's Instagram.

Mastodon (@INGVambiente@mastodon.uno) **and X** (@INGVambiente)

Particularly on these platforms, which attract a more scientifically oriented audience familiar with the department's topics, all solar flares and related events were reported. For each event, maps showing radio wave attenuation below 30 MHz and images captured by NASA satellites were provided. The language used was rather dry and technical, aimed at an audience either familiar with the field and the published content.

Facebook (https://www.facebook.com/INGVambiente) **and Instagram** (@INGVambiente)

On Facebook, it was decided to provide less technical and more sporadic information, highlighting only the most significant events in an engaging manner for the followers of the social platform. Similarly, on Instagram, one post was published in the days leading up to the storm to report the increase in solar activity, and another post on 11 May about the auroras. Within the context of the post, followers were invited to send their photos of the auroras to the INGVambiente editorial team. The received pictures were published in a carousel in Instagram Stories and highlighted among the featured stories. Each photo was accompanied by the location and the name of the author (see a selection reported in Fig. 11).

5.2 Aurora vs. Stable Auroral Arcs

Since the commencement of the main phase of the storm, reports from all over the world reported polar aurora observations, both on the social media and on mass media. Figure 12 shows a map prepared by the "Space Weather Watch" page on X (@spacewxwatch), which shows locations on Earth where at least an observation of aurora was reported.

These observations seem to span an exceptionally wide latitude range, nearly reaching the equatorial region. Although the storm was very intense, it cannot be compared to events such as the Carrington event, or one of the huge storms featuring the XIX century. The effects of those storms on the Earth's magnetic field and ionosphere were significantly stronger, with detailed observations of auroras reported even in Italy [Berrilli and Giovannelli, 2022].

Was the auroral oval really so wide during the Mother's Day storm? To assess the extent of the auroral oval, the Oval Variation, Assessment, Tracking, Intensity, and Online Nowcasting (OVATION) model [Newell et al., 2009; Machol et al., 2012] offers a detailed understanding of the auroral oval's extension in the Northern Hemisphere during such an event. Figure 13 shows the output of OVATION for the conditions during the main phase of the

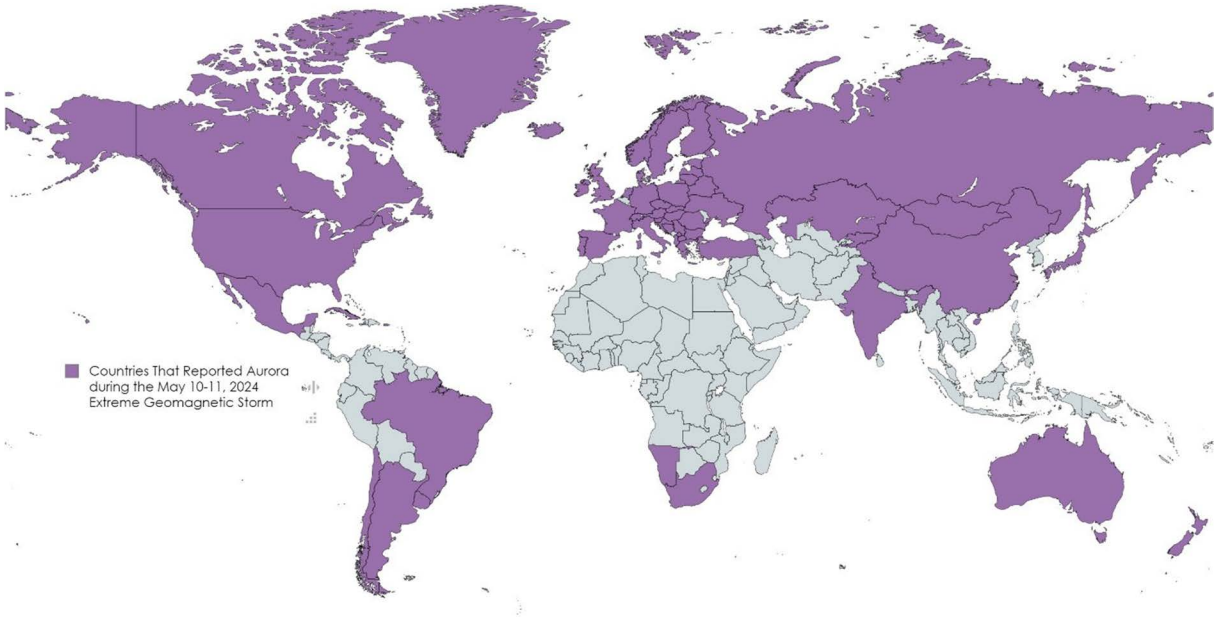

Figure 12. Places on Earth where at least an observation of aurora was reported according to the "Space Weather Watch" page on X (@spacewxwatch).

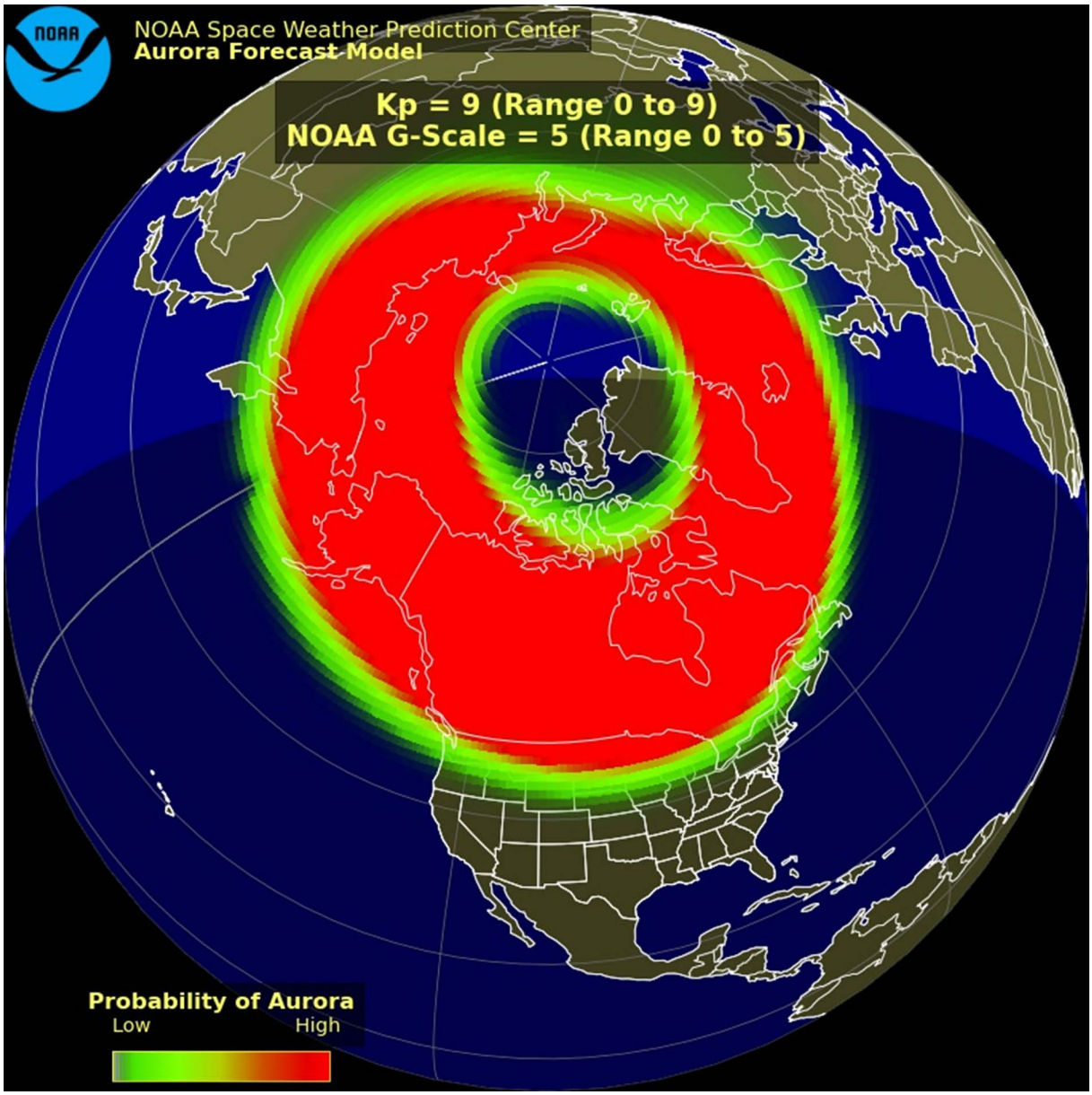

Figure 13. Output of OVATION for the conditions during the main phase of the Mother's Day storm.

storm. According to the OVATION model, the oval extended to the Southernmost part of Scandinavia and possibly the Northernmost regions of Scotland. Despite the limitations inherent in any model, it appears highly improbable that auroras could have been visible as far South as Italy or even Africa.

Nevertheless, peculiar glows in the shades of red and violet were indeed observed across various regions. Similar phenomena have been reported during past storms that were weaker than the Mother's Day storm.

The explanation proposed by many suggests the involvement of SAR arcs, which, as discussed in Section 4, are associated with the dynamics of the plasmasphere and the ring current during storm times. SAR arcs are known to produce red glows and are typically observed at lower latitudes than typical auroras. Given their characteristics, SAR arcs could indeed account for the red and violet glows observed across a wide range of latitudes during the Mother's Day storm, including regions as far South as Italy.

5.3 Issuing of the INGV Space Weather bulletin

The SWMG group is involved in a rigorous process aimed at producing a weekly bulletin that summarises Space Weather conditions that occurred during the week preceding the date of issue, with a special focus on the effects

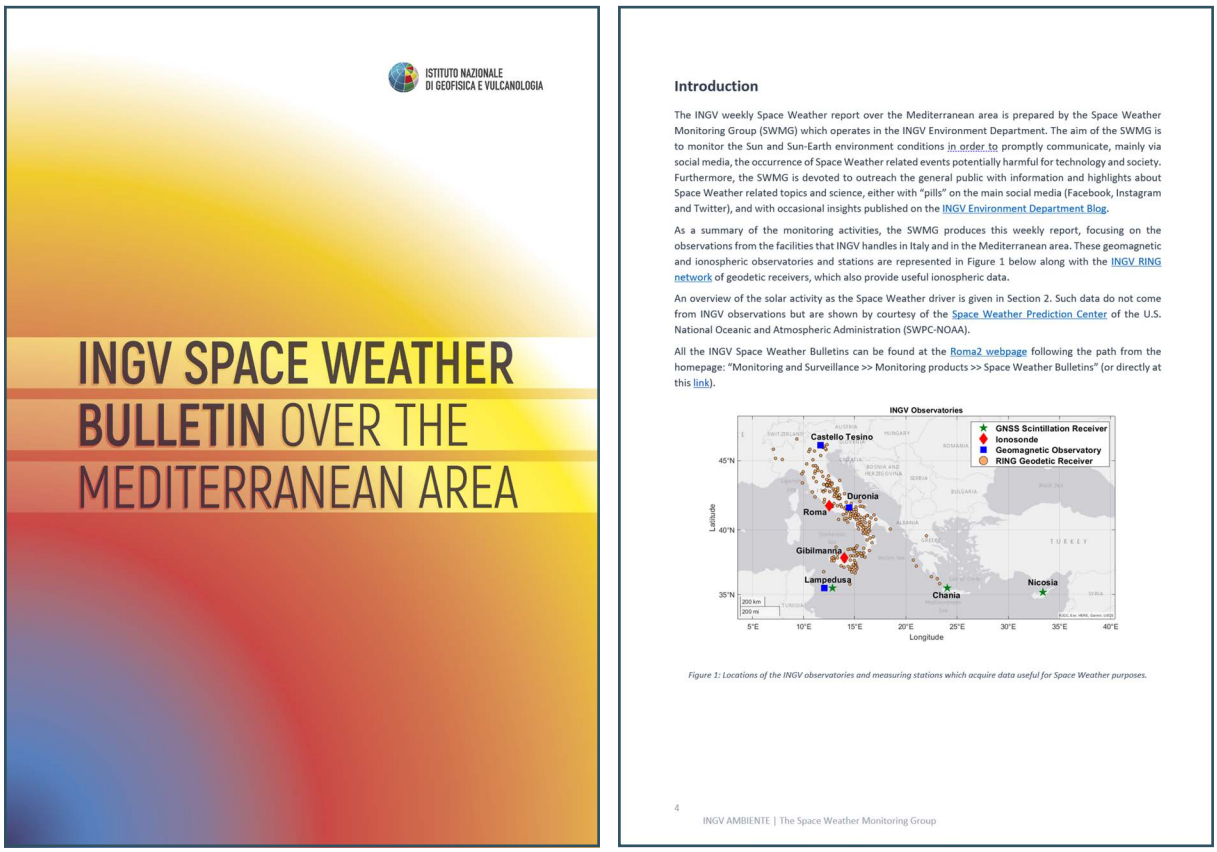

Figure 14. Cover page of the weekly INGV Space Weather Bulletin over the Mediterranean Area (left), along with the introductory page introducing the Space Weather Monitor Group (SWMG) and its activities, with a brief description of the content of the bulletin, the networks of geomagnetic and ionospheric data, and the bulletin website (right).

that may impact the Mediterranean area (Fig. 14). This bulletin provides an overview of the recently observed Space Weather conditions, highlighting potential implications that may continue to impact during the week of issuing.

Such an overview is generated after considering data from major satellite providers such as NOAA's GOES and NASA's DSCOVR and ACE missions. These satellites monitor solar activity, including solar flares, CMEs and their interplanetary counterpart (ICMEs), and SW parameters, along with the conditions of the IMF and the solar proton flux. Satellite data are complemented and compared to ground-based observations, both through ionospheric and geomagnetic data recorded by the facilities at the observatories managed by INGV in the Mediterranean area. Specifically, data from ionosondes and GNSS networks in Italy provide critical ionospheric measurements, including *fo*F2 automatically scaled from digital ionograms, TEC and ionospheric scintillation, which indicate the ionosphere's response to solar and geomagnetic activity, revealing its anomalies and disruptions. The status of the geomagnetic field is supplied by magnetometers installed in Italy and integrated into global networks. These data help track geomagnetic storms and substorms caused by solar wind-magnetosphere interactions. Geomagnetic data are processed to detect variations and perturbations in the Earth's magnetic field observed across the Italian territory, also tracking geomagnetic indices like Kp, local K (based on Duronia geomagnetic observatory dataset), and Dst.

The bulletin preparation involves synthesising the collected and analysed data into a coherent narrative. This includes current conditions, significant events, data visualisations, histograms, maps, and graphs. Each section is devoted to a specific data type, following a brief description of the data themselves, their visual representation and treatment. Critical values or variations against median conditions are carefully addressed for most of the parameters, according to proper thresholds commonly used by the scientific community or considered significant to highlight potential effects, and a list of significant events is reported in each section. A summary of the week is placed at the beginning of the bulletin to highlight the most relevant events, with the help of a visual overview. As an example, in Figure 15 the overview of the time intervals in which out-of-threshold events of different nature (red boxes) were

detected during the week of the storm, from 6 to 12 May is reported. This allows the identification of strong solar flares during the whole week, and the occurrence of the geomagnetic storm, along with its ionospheric effects over the Mediterranean area.

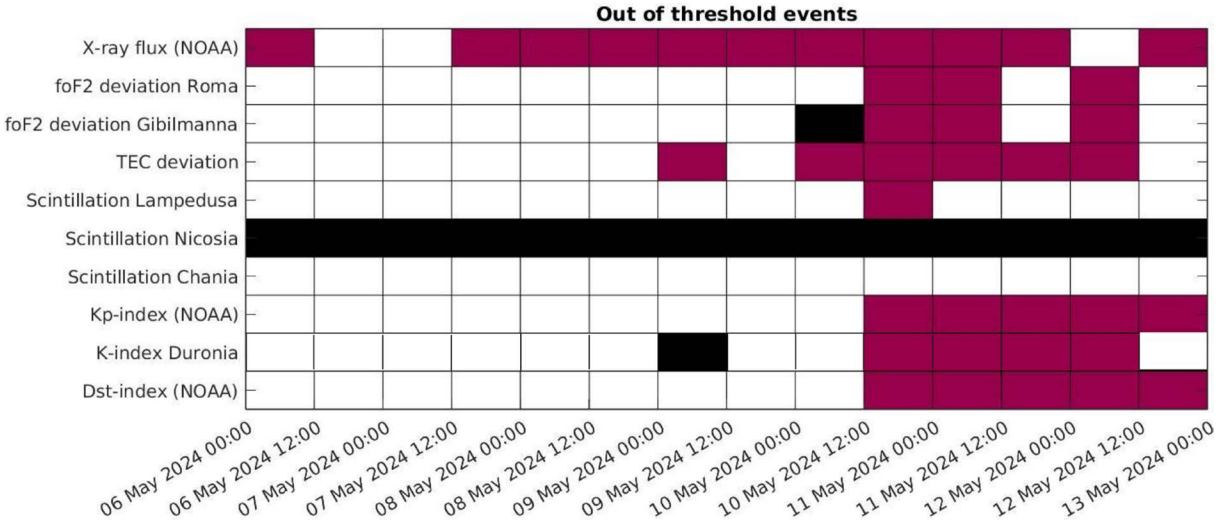

Figure 15. Overview of the out-of-threshold events (red boxes) and lack of data (black ones) occurred during the week of the storm, from 6 to 12 May, included in the corresponding issue of the weekly INGV Space Weather Bulletin over the Mediterranean Area (Issue nr. 20/2024).

The bulletin is compiled to ensure clarity and accuracy. It is peer-reviewed within the team to validate the findings. The final bulletin is made available to the public through our website (https://roma2.ingv.it/index.php/monitoraggio-e-sorveglianza/prodotti-del-monitoraggio/bollettini-di-space-weather) and other communication channels, including social media. The goal of this bulletin is to raise general public awareness on Space Weather as well as specialised stakeholders, such as civil protection agencies and other actors responsible for managing public risks.

6. Conclusions: an extreme storm in the contemporary technological era

The Sun is nearing the maximum of its 25th cycle of activity. A strong contribution to its activity in May came from the active region AR13664. At the time the event under study was triggered, it had an extension of 2400 millionths of a solar hemisphere (MH), that is about 0.24% of the Earth-facing solar surface and comparable with the size of the active region that originated the extreme Carrington event in 1859. By comparison, the typical size of a sunspot group is less than 200 MH. AR13664 gave rise to several X-class flares, two of which entered the list of the 50 most intense flares of the last 30 years, accompanied by several ICMEs. The interaction of this large amount of energy ejected from the Sun with the circumterrestrial environment triggered the 2024 Mother's Day superstorm, the most intense storm since the Halloween and November storms in 2003. We focused on the effects that this storm had on the Mediterranean and, more specifically, over the Italian region.

The notable phenomena occurring during the storm can be summarised as follows:

1) very steep SSC and maximum variations in the horizontal component of the geomagnetic field over Italy of the order of 600 nT;
2) a significant depression of the ionospheric plasma, as testified by the very low values of *fo*F2 and vTEC over Italy reaching 2 MHz and 4 TECu, respectively, corresponding to a decrease of about 70% with respect to quiet conditions. This is a situation that has characterised two whole days, the 11 and the 13 May, and ascribed to a decrease of the [O]/[N_2] ratio, reaching very low values down to 0.2 during those days (33% of the value measured on 8 May);

3) a significant upward displacement of the ionosphere with respect to the quiet conditions, testified by an increase of the *hm*F2 over the Rome station and confirmed by the background plasma density measured by Swarm B flying well below the F region in the latitudinal range 0° to 20° N;
4) high and unusual spatially distributed ROTI values characterised the nights of 10 and 11 May. An important result of the study is that ROTI enhancements on 10 May, along with co-located impressive plasma temperature enhancements measured by Swarm B spacecraft, might be partly ascribed to the same physical mechanism generating the SAR arcs, which, as far as we are concerned, is interesting and quite intriguing. ROTI enhancements recorded on 11 May seem to be the result of a joint action of low-latitude plasma shifted by the PRE and wave-like perturbations coming from the north resulting in a large-scale mid-latitude plasma blob oriented in the NW-SE direction;
5) the IRI UP IONORING, which is the model assimilating IONORING TEC maps into the IRI model, recently developed at INGV to nowcast *fo*F2 over Italy, for this important event proved its reliability during an extreme event.

Moreover, this storm immediately caught the attention of the public, who reported sightings of phenomena like SAR arcs. This gives scientists an important opportunity to correctly inform the public about the most fascinating aspects of solar storms, while also making them aware of the problems that this type of event can cause, especially in critical areas like the Mediterranean one. This is a task that in the last two years the Space Weather Monitoring Group of INGV Environment Department has begun to carry out through various activities described in the paper.

This event taught us that we must not let our guard down. The international scientific community must continue to understand these phenomena more deeply, while setting up monitoring centres capable of providing the civil society with the most reliable alerts possible. The more prepared we are, the better we will be able to deal with even more intense events, limiting damage to infrastructure, and consequently, minimising economic losses.

Data and sharing resources. Data and products available in the eSWua data portal (www.eswua.ingv.it) can be downloaded by using the download tools (http://eswua.ingv.it/index.php/data-access-and-info/download-tool) or via the dedicated web service (http://eswua.ingv.it/index.php/data-access-and-info/web-service).
The digital archive of the Italian geomagnetic observatory data (doi.org/10.13127/GEOMAG/RAWDATA) and products can be freely accessed from the data portal at geomag.rm.ingv.it under the "download area" subpages.
The SDO data used in this work are available from the SDO database (https://sdo.gsfc.nasa.gov/data/aiahmi/).
The CACTus CME catalogue used in this study may be retrieved from https://www.sidc.be/cactus/.
IRI UP uses the IRI model as background. IRI Fortran code is available via the IRI website (http://irimodel.org/).
RINEX data from the RING network are available on the INGV FTP repository at ftp://gpsfree.gm.ingv.it.
RINEX data from the EUREF network are available on the ROB repository at https://epncb.eu/pub/obs/.
Swarm data are provided by the European Space Agency (ESA) through FTP and HTTP Servers at https://earth.esa.int/eogateway/missions/swarm/data.
TIMED-GUVI [O]/[N2] data are available on the Johns Hopkins University Applied Physics Laboratory website at https://guvitimed.jhuapl.edu/index.php/.
DSCOVR data are available at National Centers for Environmental Information of NOAA (https://www.ngdc.noaa.gov/dscovr/portal/index.html#/).
Kp data are available at https://dataservices.gfz-potsdam.de/panmetaworks/showshort.php?id=escidoc:5216888
GOES-16 data are available at: https://www.ngdc.noaa.gov/stp/satellite/goes-r.html.
Dst index data: https://wdc.kugi.kyoto-u.ac.jp/dstdir/.
The CIRES Equatorial Electric Field Model is available at https://geomag.colorado.edu/ppeef.html
The FMI-IMAGE electrojet indicators are available at https://space.fmi.fi/image/www/index.php.
OVATION model maps are freely available at National Centers for Environmental Information of NOAA (https://www.swpc.noaa.gov/products/aurora-30-minute-forecast).

Acknowledgements. Authors are grateful to Luigi "Gg" Ciraolo for the provision of the TEC calibration and the precious discussions about it. Authors thank Lucilla Alfonsi, Paola De Michelis and Marco Pietrella for the valuable discussions, Enrico Zuccheretti for the support for and management of the INGV AIS Ionosondes and fruitful discussion about HF

data, and Andrea Malagnini for his help in manually scaling the ionograms. Authors thank Filippos Vallianatos for the support with ISMR in Chania, Greece and Alcide Giorgio di Sarra (scientific director of the activities at the ENEA Climate Observation Station) and Damiano Sferlazzo for the support in managing the GNSS receiver in Lampedusa.
We acknowledge the use of DSCOVR data provided by the National Oceanic and Atmospheric Administration (NOAA) and the National Aeronautics and Space Administration (NASA). We also acknowledge the Working Earth (Pianeta Dinamico) Project for Monte Crisimo (and Serra Pizzuta) magnetic data.
The Space Weather Monitoring Group (SWMG) of INGV Environment Department is thanked for its efforts in disseminating the weekly Space Weather bulletin, which is freely available for consultation and download.
We thank the institutes who maintain the IMAGE Magnetometer Array: Tromsø Geophysical Observatory of UiT the Arctic University of Norway (Norway), Finnish Meteorological Institute (Finland), Institute of Geophysics Polish Academy of Sciences (Poland), GFZ German Research Centre for Geosciences (Germany), Geological Survey of Sweden (Sweden), Swedish Institute of Space Physics (Sweden), Sodankylä Geophysical Observatory of the University of Oulu (Finland), DTU Technical University of Denmark (Denmark), and Science Institute of the University of Iceland (Iceland). The provisioning of data from AAL, GOT, HAS, NRA, VXJ, FKP, SIN, BOR, SCO and KUL is supported by the ESA contracts number 4000128139/19/D/CT as well as 4000138064/22/D/KS.
The results presented in this paper rely on geomagnetic indices calculated and made available by ISGI Collaborating Institutes from data collected at magnetic observatories. We thank the involved national institutes, the INTERMAGNET network and ISGI (isgi.unistra.fr).
IRI UP uses the IRI model as background. The authors acknowledge the IRI team for developing and maintaining the IRI model and for giving access to the corresponding Fortran code via the IRI website (http://irimodel.org/).
The GUVI data used here are provided through support from the NASA MO&DA program. The GUVI instrument was designed and built by The Aerospace Corporation and The Johns Hopkins University. The Principal Investigator is Dr. Larry J. Paxton.

References

Alfonsi, L., L. Spogli, J.R. Tong, G. De Franceschi, V. Romano, A. Bourdillon, M. Le Huy and C.N. Mitchell (2011). GPS scintillation and TEC gradients at equatorial latitudes in April 2006, Adv. Space Res., 47, 10, 1750-1757. https://doi.org/10.1016/j.asr.2010.04.020

Alfonsi, L., C. Cesaroni, L. Spogli, M. Regi, A. Paul, S. Ray, S. Lepidi, D. Di Mauro, H. Haralambous, C. Oikonomou, P.R. Shreedevi and A.K. Sinha (2021). Ionospheric disturbances over the Indian sector during 8 September 2017 geomagnetic storm: Plasma structuring and propagation, Space Weather, 19(3), e2020SW002607. https://doi.org/10.1029/2020SW002607

Astafyeva, E., I. Zakharenkova and M. Förster (2015). Ionospheric response to the 2015 St. Patrick's Day storm: A global multi-instrumental overview, J. Geophys. Res. Space Phys., 120, 10, 9023-9037. https://doi.org/10.1002/2015JA021629

Astafyeva, E., I. Zakharenkova, J.D. Huba, E. Doornbos and J. Van den IJssel (2017). Global ionospheric and thermospheric effects of the June 2015 geomagnetic disturbances: Multi-instrumental observations and modeling, J. Geophys. Res. Space Phys., 122, 11, 11,716-11,742. https://doi.org/10.1002/2017JA024174

Astafyeva, E., Y.V. Yasyukevich, B. Maletckii, A. Oinats, A. Vesnin, A.S.S. Yasyukevich, S. Syrovatskii and N. Guendouz (2022). Ionospheric disturbances and irregularities during the 25-26 August 2018 geomagnetic storm, J. Geophys. Res. Space Phys., 127, 1, e2021JA029843. https://doi.org/10.1029/2021JA029843

Benz, A.O. (2017). Flare Observations, Living Rev. Solar Phys., 14, 1. 10.1007/s41116-016-0004-3

Berrilli, F. and L. Giovannelli (2022). The Great Aurora of 4 February 1872 observed by Angelo Secchi in Rome, J. Space Weather Space Climate, 12, 3. https://doi.org/10.1051/swsc/2021046

Bilitza, D., M. Pezzopane, V. Truhlik, D. Altadill, B.W. Reinisch and A. Pignalberi (2022). The International Reference Ionosphere model: A review and description of an ionospheric benchmark, Rev. Geophys., 60, e2022RG000792. https://doi.org/10.1029/2022RG000792

Bougard, B., J.M. Sleewaegen, L. Spogli, S.V. Veettil and J.F. Monico (2011). CIGALA: Challenging the solar maximum in Brazil with PolaRxS, in proceedings of the 24th International Technical Meeting of the Satellite Division of the Institute of Navigation (ION GNSS 2011), Portland, OR, 2572-2579.

Bruyninx, C., J. Legrand, A. Fabian and E. Pottiaux (2019). GNSS metadata and data validation in the EUREF Permanent Network, GPS Sol., 23. https://doi.org/10.1007/s10291-019-0880-9

Buonsanto, M. (1999). Ionospheric storms—a review, Space Sci. Rev., 88, 3, 563-601. https://doi.org/10.1023/A:1005107532 631

Burt, J. and B. Smith (2012). Deep Space Climate Observatory: The DSCOVR mission, in proceedings of the IEEE Aerospace Conference, Big Sky, MT, USA, 1-13. https://doi.org/10.1109/AERO.2012.6187025

Catapano, F., S. Buchert, E. Qamili, T. Nilsson, J. Bouffard, C. Siemes, I. Coco, R. D'Amicis, L. Tøffner-Clausen, L. Trenchi, P.E. Holmdahl Olsen and A. Stromme (2022). Swarm Langmuir probes' data quality validation and future improvements, Geosc. Instr. Meth. Data Syst., 11, 149-162. https://doi.org/10.5194/gi-11-149-2022

Cesaroni, C., L. Alfonsi, M. Pezzopane, C. Martinis, J. Baumgardner, J. Wroten, M. Mendillo, E. Musicò and G. Umbriaco (2017). The First Use of Coordinated Ionospheric Radio and Optical Observations Over Italy: Convergence of High-and Low-Latitude Storm-Induced Effects, J. Geophys. Res. Space Phys., 122, 11, 11-794. https://doi.org/10.1002/2017JA024325

Cesaroni, C., L. Spogli and G. De Franceschi (2021). IONORING: real-time monitoring of the total electron content over Italy, Rem. Sens., 13, 16, 3290. https://doi.org/10.3390/rs13163290

Cherniak, I., I. Zakharenkova and R.J. Redmon (2015). Dynamics of the high-latitude ionospheric irregularities during the 17 March 2015 St. Patrick's Day storm: Ground-based GPS measurements, Space Weather, 13, 9, 585-597. https://doi.org/10.1002/2015SW001237

Cherniak, I. and I. Zakharenkova (2017). New advantages of the combined GPS and GLONASS observations for high-latitude ionospheric irregularities monitoring: case study of June 2015 geomagnetic storm, Earth Plan. Space, 69, 1-14. https://doi.org/10.1186/s40623-017-0652-0

Christensen, A.B., L.J. Paxton, S. Avery, J. Craven, G. Crowley, D.C. Humm, H. Kil, R.R. Meier, C.-I. Meng, D. Morrison, B.S. Ogorzalek, P. Straus, D.J. Strickland, R.M. Swenson, R.L. Walterscheid, B. Wolven and Y.L. Zhang (2003). Initial observations with the Global Ultraviolet Imager (GUVI) in the NASA TIMED satellite mission, J. Geophys. Res. Space Phys., 108, A12. https://doi.org/10.1029/2003JA009918

D'Angelo, G., L. Spogli, C. Cesaroni, V. Sgrigna, L. Alfonsi and M.H.O. Aquino (2015). GNSS data filtering optimization for ionospheric observation, Adv. Space Res., 56, 11, 2552-2562. https://doi.org/10.1016/j.asr.2015.10.002

Deminov, M.G., E.B. Romanova and A.V. Tashchilin (2011). Origination of G conditions in the ionospheric F region depending on solar and geomagnetic activity, Geom. Aeron., 51, 5, 669. https://doi.org/10.1134/S0016793211050045

Fletcher, L. (2011). An Observational Overview of Solar Flares, Space Sci. Rev., 159, 1-4, 19-106. https://doi.org/10.1007/s11214-010-9701-8

Fremouw, E.J., R.L. Leadabrand, R.C. Livingston, M.D. Cousins, C.L. Rino, B.C. Fair and R.A. Long (1978). Early results from the DNA Wideband satellite experiment—Complex-signal scintillation, Radio Sci., 13, 1, 167-187. https://doi.org/10.1029/RS013i001p00167

Friis-Christensen, E., H. Lühr, D. Knudsen and R. Haagmans (2008). Swarm—An Earth Observation Mission investigating Geospace, Adv. Space Res., 41, 210-216. https://doi.org/10.1016/j.asr.2006.10.008

Gallardo-Lacourt, B., H.U. Frey and C. Martinis (2021). Proton Aurora and Optical Emissions in the Subauroral Region, Space Sci. Rev., 217, 10. https://doi.org/10.1007/s11214-020-00776-6

Ghobadi, H., L. Spogli, L. Alfonsi, C. Cesaroni, A. Cicone, N. Linty, V. Romano and M. Cafaro (2020). Disentangling ionospheric refraction and diffraction effects in GNSS raw phase through fast iterative filtering technique, GPS Sol., 24, 85. https://doi.org/10.1007/s10291-020-01001-1

Gopalswamy, N., S. Yashiro, G. Michalek, H. Xie, R.P. Lepping and R.A. Howard (2005). Solar source of the largest geomagnetic storm of cycle 23, Geophys. Res. Lett., 32, 12. https://doi.org/10.1029/2004GL021639

Gopalswamy, N. (2006). Properties of interplanetary coronal mass ejections, Space Sci. Rev., 124, 145-168. https://doi.org/10.1007/s11214-006-9102-1

Gosling, J.T., E. Hildner, R.M. MacQueen, R.H. Munro, A.I. Poland and C.L. Ross (1976). The speeds of coronal mass ejection events, Sol. Phys., 48, 2, 389-397. 10.1007/BF00152004

Hibberd, F.H. and W.J. Ross (1966). Total electron content of the ionosphere in middle latitudes. J. Geophys. Res., 71, 9, 2243-2253. https://doi.org/10.1029/JZ071i009p02243

Hirayama, T. (1974). Theoretical Model of Flares and Prominences. I: Evaporating Flare Model, Sol. Phys., 34, 323-338. https://doi.org/10.1007/BF00153671

INGV RING Working Group (2016). Rete Integrata Nazionale GPS (RING) [Data set]. Istituto Nazionale di Geofisica e Vulcanologia (INGV). https://doi.org/10.13127/ring

Ippolito, A., P. Pommois, G. Zimbardo and P. Veltri (2005). Magnetic connection from the Earth to the solar corona, flare positions and solar energetic particle observations, Astr. Astrophys., 438, 705-711. https://doi.org/10.1051/0004-6361:20052776

Kauristie, K., J. Andries, P. Beck, J. Berdermann, D. Berghmans, C. Cesaroni, E. De Donder, J. de Patoul, M. Dierckxsens, E. Doornbos, M. Gibbs, K. Hammond, H. Haralambous, A.-M. Harri, E. Henley, M. Kriegel, T. Laitinen, M. Latocha, Y. Maneva, L. Perrone, E. Pica, L. Rodriguez, V. Romano, D. Sabbagh, L. Spogli, I. Stanislawska, L. Tomasik, M. Tshisaphungo, K. Kasper van Dam, B. van den Oord, P. Vanlommel, T. Verhulst, V. Wilken, A. Zalizovski and K. Österberg (2021). Space weather services for civil aviation—Challenges and solutions, Rem. Sens., 13, 18, 3685. https://doi.org/10.3390/rs13183685

Kil, H., L.J. Paxton, G. Jee and R. Nikoukar (2019). Plasma blobs associated with medium-scale traveling ionospheric disturbances, Geophys. Res. Lett., 46, 7, 3575-3581. https://doi.org/10.1029/2019GL082026

Kim, J., Y.S. Kwak, C. Lee, J. Lee, H. Kam, T.Y. Yang, G. Jee and Y. Kim (2023). Observational evidence of thermospheric wind and composition changes and the resulting ionospheric disturbances in the European sector during extreme geomagnetic storms, J. Space Weather Space Clim., 13, 24. https://doi.org/10.1051/swsc/2023025

Knudsen, D.J., J.K. Burchill, S.C. Buchert, A.I. Eriksson, R. Gill, J.E. Wahlund, L. Åhlen, M. Smith and B. Moffat (2017). Thermal ion imagers and Langmuir probes in the Swarm electric field instruments, J. Geophys. Res. Space Phys., 122, 2655-2673, https://doi.org/10.1002/2016JA022571.

Kozyra, J.U., E.G. Shelley, R.H. Comfort, L.H. Brace, T.E. Cravens and A.F. Nagy (1987). The role of ring current O^+ in the formation of stable red arcs, J. Geophys. Res., 92, 7487. https://doi.org/10.1029/JA092iA07p07487

Li, C., C.M. Hancock, S. Vadakke Veettil, D. Zhao, J.F. Galera Monico and N.A. Hamm (2022). Distinguishing ionospheric scintillation from multipath in GNSS signals using geodetic receivers, GPS Sol., 26, 4, 150. https://doi.org/10.1007/s10291-022-01328-x

Linty, N., A. Minetto, F. Dovis and L. Spogli (2018). Effects of phase scintillation on the GNSS positioning error during the September 2017 storm at Svalbard, Space Weather, 16, 9, 1317-1329. https://doi.org/10.1029/2018SW001940

Lopez, R.E., D.N. Baker and J. Allen (2004). Sun unleashes Halloween storm, Eos, Trans. American Geophys. Union, 85, 11, 105-108. https://doi.org/10.1029/2004EO110002

Lotoaniu, P.T., K. Romich, W. Rowland, S. Codrescu, D. Biesecker, J. Johnson, H.J. Singer, A. Szabo and M. Stevens (2022). Validation of the DSCOVR spacecraft mission space weather solar wind products, Space Weather, 20, 10, e2022SW003085. https://doi.org/10.1029/2022SW003085

Lühr, H., J. Park, J.W. Gjerloev, J. Rauberg, I. Michaelis, J.M. Merayo and P. Brauer (2015). Field-aligned currents' scale analysis performed with the Swarm constellation, Geophys. Res. Lett., 42, 1, 1-8. https://doi.org/10.1002/2014GL062453

Machol, J.L., J.C. Green, R.J. Redmon, R.A. Viereck and P.T. Newell (2012). Evaluation of OVATION Prime as a forecast model for visible aurorae, Space Weather, 10, 3. https://doi.org/10.1029/2011SW000746

Manoj, C., S. Maus and P. Alken (2013), Long-period prompt-penetration electric fields derived from CHAMP satellite magnetic measurements, J. Geophys. Res. Space Phys., 118, 5919-5930. https://doi.org/10.1002/jgra.50511

Manoj, C. and S. Maus (2012). A real-time forecast service for the ionospheric equatorial zonal electric field, Space Weather, 10, S09002. https://doi.org/10.1029/2012SW000825

Manoj, C., S. Maus, H. Lühr and P. Alken (2008). Penetration characteristics of the interplanetary electric field to the daytime equatorial ionosphere, J. Geophys. Res. Space Phys., 113, A12310. https://doi.org/10.1029/2008JA013381

Matzka, J., C. Stolle, Y. Yamazaki, O. Bronkalla and A. Morschhauser (2021). The geomagnetic Kp index and derived indices of geomagnetic activity, Space Weather, 19, e2020SW002641. https://doi.org/10.1029/2020SW002641

Mayaud, P.N. (1980). Derivation, Meaning, and Use of Geomagnetic Indices, Geophys. Monograph Series, Volume 22, American Geophys. Union, ISBN:9780875900223. https://doi.org/10.1029/GM022

Mendillo, M. (2006). Storms in the ionosphere: Patterns and processes for total electron content, Rev. Geophys., 44, 4. https://doi.org/10.1029/2005RG000193

Mrak, S., A.J. Coster, K. Groves and R. Nikoukar (2023). Ground-based infrastructure for monitoring and characterizing intermediate-scale ionospheric irregularities at mid-latitudes, Front. Astron. Space Sci., 10, 1091340. https://doi.org/10.3389/fspas.2023.1091340

Musico, E., C. Cesaroni, L. Spogli, J.P.M. Boncori, G. De Franceschi and R. Seu (2018). The Total Electron Content from InSAR and GNSS: a midlatitude study, IEEE J. Sel. Topics Appl. Earth Observ. Rem. Sens., 11, 5, 1725-1733. 10.1109/JSTARS.2018.2812305

Nava, B., J. Rodríguez-Zuluaga, K. Alazo-Cuartas, A. Kashcheyev, Y. Migoya-Orué, S.M. Radicella, C. Amory-Mazaudier and R. Fleury (2016). Middle-and low-latitude ionosphere response to 2015 St. Patrick's Day geomagnetic storm, J. Geophys. Res. Space Phys., 121, 4, 3421-3438. https://doi.org/10.1002/2015JA022299

Newell, P.T., T. Sotirelis and S. Wing (2009). Diffuse, monoenergetic, and broadband aurora: The global precipitation budget, J. Geophys. Res. Space Phys., 114, A09207. https://doi.org/10.1029/2009JA014326

Park, J., C.S. Huang, R.W. Eastes and A.J. Coster (2022). Temporal evolution of low-latitude plasma blobs identified from multiple measurements: ICON, GOLD, and Madrigal TEC, J. Geophys. Res. Space Phys., 127, 3, e2021JA029992. https://doi.org/10.1029/2021JA029992

Pesnell, W.D., B.J. Thompson and P.C. Chamberlin (2011). The Solar Dynamics Observatory (SDO), in The Solar Dynamics Observatory Chamberlin, P., W. D. Pesnell and B. Thompson (Editors), Springer, New York. https://doi.org/10.1007/978-1-4614-3673-7_2

Perrone, L. and A.V. Mikhailov (2018). A new method to retrieve thermospheric parameters from daytime bottom-side Ne (h) observations, J. Geophys. Res. Space Phys., 123, 12, 10-200. https://doi.org/10.1029/2018JA025762

Pezzopane, M. (2004). Interpre: A Windows software for semiautomatic scaling of ionospheric parameters from ionograms, Comp. Geosci., 30, 1, 125-130. https://doi.org/10.1016/j.cageo.2003.09.009

Pezzopane, M., A. Del Corpo, M. Piersanti, C. Cesaroni, A. Pignalberi, S. Di Matteo, L. Spogli, M. Vellante and B. Heilig (2019). On some features characterizing the plasmasphere–magnetosphere–ionosphere system during the geomagnetic storm of 27 May 2017, Earth Plan. Space, 71, 1, 77. https://doi.org/10.1186/s40623-019-1056-0

Pi, X., A.J. Mannucci, U.J. Lindqwister and C.M. Ho (1997). Monitoring of global ionospheric irregularities using the worldwide GPS network, Geophys. Res. Lett., 24, 18, 2283-2286. https://doi.org/10.1029/97GL02273

Pica, E., C. Marcocci, C. Cesaroni, E. Zuccheretti, M. Pezzopane, S. Vecchi, V. Romano and L. Spogli (2021). The SWIT-eSWua system: managing, preservation and sharing of the historical and near real-time ionospheric data at the INGV, ESS Open Archive. 10.1002/essoar.10506618.1

Piersanti, M., T. Alberti, A. Bemporad, F. Berrilli, R. Bruno, V. Capparelli, V. Carbone, C. Cesaroni, G. Consolini, A. Cristaldi, A. Del Corpo, D. Del Moro, S. Di Matteo, I. Ermolli, S. Fineschi, F. Giannattasio, F. Giorgi, L. Giovannelli, S.L. Guglielmino, M. Laurenza, F. Lepreti, M.F. Marcucci, M. Martucci, M. Mergè, M. Pezzopane, E. Pietropaolo, P. Romano, R. Sparvoli, L. Spogli, M. Stangalini, A. Vecchio, M. Vellante, U. Villante, F. Zuccarello, B. Heilig and J. Lichtenberger (2017). Comprehensive analysis of the geoeffective solar event of 21 June 2015: effects on the magnetosphere, plasmasphere, and ionosphere systems, Sol. Phys., 292, 1-56. https://doi.org/10.1007/s11207-017-1186-0

Pignalberi, A., M. Pezzopane, R. Rizzi and I. Galkin (2018). Effective solar indices for ionospheric modeling: A review and a proposal for a real-time regional IRI, Surv. Geophys., 39, 1, 125-167. https://doi.org/10.1007/s10712-017-9438-y

Pignalberi, A., J.B. Habarulema, M. Pezzopane and R. Rizzi (2019). On the development of a method for updating an empirical climatological ionospheric model by means of assimilated vTEC measurements from a GNSS receiver network, Space Weather, 17, 7, 1131-1164. https://doi.org/10.1029/2019SW002185

Pignalberi, A., B. Nava, M. Pietrella, C. Cesaroni and M. Pezzopane (2021). Mid-latitude climatology of the ionospheric equivalent slab thickness over two solar cycles, J. Geod., 95, 124. https://doi.org/10.1007/s00190-021-01577-7

Pignalberi, A., M. Pietrella, M. Pezzopane, B. Nava and C. Cesaroni (2022). The Ionospheric Equivalent Slab Thickness: A Review Supported by a Global Climatological Study Over Two Solar Cycles, Space Sci. Rev., 218, 37. https://doi.org/10.1007/s11214-022-00909-z

Pignalberi, A., C. Cesaroni, M. Pietrella, M. Pezzopane, L. Spogli, C. Marcocci and E. Pica. (2024a). Ionospheric nowcasting over Italy through data assimilation: A synergy between IRI UP and IONORING, Space Weather, 22, e2023SW003838. https://doi.org/10.1029/2023SW003838

Pignalberi, A., B. Nava, M. Pietrella, M. Pezzopane, P. Coïsson and C. Cesaroni (2024b). Ionospheric equivalent slab thickness ingestion into the NeQuick model, Ann. Geophys., 66, 5, PA528. 10.4401/ag-9026

Pignalberi, A., V. Truhlik, F. Giannattasio, I. Coco and M. Pezzopane (2024c). Mid-and High-Latitude Electron Temperature Dependence on Solar Activity in the Topside Ionosphere through the Swarm B Satellite Observations and the International Reference Ionosphere Model, Atmosphere, 15, 4, 490. https://doi.org/10.3390/atmos15040490

Prölss, G.W. (1995). Ionospheric F-region storms, in Handbook of Atmospheric Electrodynamics H. Volland (Editor), CRC Press, Boca Raton, FL, USA, 195-248.

Qian, L., W. Wang, A.G. Burns, P.C. Chamberlin, A. Coster, S.R. Zhang and S.C. Solomon (2019). Solar flare and geomagnetic storm effects on the thermosphere and ionosphere during 6-11 September 2017, J. Geophys. Res. Space Phys., 124, 3, 2298-2311. https://doi.org/10.1029/2018JA026175

Reames, D.V. (2013). The Two Sources of Solar Energetic Particles, Space Sci. Rev., 175, 53. https://doi.org/10.1007/s11214-013-9958-9

Regi, M., P. Bagiacchi, D. Di Mauro, S. Lepidi, and L. Cafarella (2020). On the validation of K-index values at Italian geomagnetic observatories, Geosc. Instr. Meth. Data Syst., 9, 1. https://doi.org/10.5194/gi-9-105-2020

Regi, M., L. Perrone, A. Del Corpo, L. Spogli, D. Sabbagh, C. Cesaroni, L. Alfonsi, P. Bagiacchi, L. Cafarella, G. Carnevale, M. De Lauretis, D. Di Mauro, P. Di Pietro, P. Francia, B. Heilig, S. Lepidi, C. Marcocci, F. Masci, A. Nardi, A. Piscini, G. Redaelli, V. Romano, U. Sciacca and C. Scotto (2022). Space weather effects observed in the Northern Hemisphere during November 2021 geomagnetic storm: The impacts on plasmasphere, ionosphere and thermosphere systems, Rem. Sens., 14, 22, 5765. https://doi.org/10.3390/rs14225765

Robbrecht, E. and D. Berghmans (2004). Automated recognition of coronal mass ejections (CMEs) in near-real time data, Astron. Astrophys., 425, 1097-1106. https://doi.org/10.1051/0004-6361:20041302

Rodrigues, F.S., J.G. Socola, A.O. Moraes, C. Martinis and D.A. Hickey (2021). On the properties of and ionospheric conditions associated with a mid-latitude scintillation event observed over southern United States, Space Weather, 19, 6, e2021SW002744. https://doi.org/10.1029/2021SW002744

Romano, V., L. Spogli, M. Aquino, A. Dodson, C. Hancock and B. Forte (2013). GNSS station characterisation for ionospheric scintillation applications, Adv. Space Res., 52, 7, 1237-1246. https://doi.org/10.1016/j.asr.2013.06.028

Scherrer, P.H., J. Schou, R.I. Bush, A.G. Kosovichev, R.S. Bogart, J.T. Hoeksema, Y. Liu, T.L. Jr Duvall, J. Zhao, A.M. Title, C.J. Schrjver, T.D. Tarbell and S. Tomczyk (2012). The helioseismic and magnetic imager (hmi) investigation for the solar dynamics observatory (sdo), Sol. Phys., 275, 1, 207. https://doi.org/10.1007/s11207-011-9834-2

Scotto, C. and M. Pezzopane (2002). A software for automatic scaling of foF2 and MUF (3000) F2 from ionograms, in proceedings of the URSI XXVIIth General Assembly, Maastricht, Holland.

Scotto, C. (2009). Electron density profile calculation technique for Autoscala ionogram analysis, Adv. Space Res., 44, 756-766. https://doi.org/10.1016/j.asr.2009.04.037

Scotto, C. and D. Sabbagh (2020). The accuracy of real-time hmF2 estimation from ionosondes, Rem. Sens., 12, 17, 2671. https://doi.org/10.3390/rs12172671

Shibata, K.C., S. Masuda, M. Shimojo, H. Hara, T. Yokoyama, S. Tsuneta, T. Kosugi and Y. Ogawara (1995). Hot Plasma Ejections Associated with Compact Loop Solar Flares, Astrophys. J., 451, 2. 10.1086/309688

Spogli, L., L. Alfonsi, V. Romano, G. De Franceschi, G.M.J. Francisco, M.H. Shimabukuro, B. Bougard and M. Aquino (2013). Assessing the GNSS scintillation climate over Brazil under increasing solar activity, J. Atmos. Sol.-Terr. Phys., 105, 199-206. https://doi.org/10.1016/j.jastp.2013.10.003

Spogli, L., C. Cesaroni, D. Di Mauro, M. Pezzopane, L. Alfonsi, E. Musicò, G. Povero, M. Pini, F. Dovis, R. Romero, N. Linty, P. Abadi, F. Niraeni, A. Husin, M. Le Huy, T.T. Lan, T.V. La, V.G. Pillat and N. Floury (2016). Formation of ionospheric irregularities over Southeast Asia during the 2015 St. Patrick's Day storm, J. Geophys. Res. Space Phys., 121, 12,211-12,233. 10.1002/2016JA023222

Spogli, L., D. Sabbagh, M. Regi, C. Cesaroni, L. Perrone, L. Alfonsi, D. Di Mauro, S. Lepidi, S.A. Campuzano, D. Marchetti, A. De Santis, A. Malagnini, C. Scotto, G. Cianchini, X.H. Shen, A. Piscini and A. Ippolito (2021). Ionospheric response over Brazil to the August 2018 geomagnetic storm as probed by CSES-01 and Swarm satellites and by local ground-based observations, J. Geophys. Res. Space Phys., 126, 2, e2020JA028368. https://doi.org/10.1029/2020JA028368

Spogli, L., L. Alfonsi and C. Cesaroni (2023). Stepping into an equatorial plasma bubble with a Swarm overfly, Space Weather, 21, 5, e2022SW003331. https://doi.org/10.1029/2022SW003331

Srivastava, N., S.K. Mathew, R.E. Louis and T. Wiegelmann (2009). Source region of the 18 November 2003 coronal mass ejection that led to the strongest magnetic storm of cycle 23, J. Geophys. Res. Space Phys., 114, A3. https://doi.org/10.1029/2008JA013845

Tanskanen, E.I. (2009). A comprehensive high-throughput analysis of substorms observed by IMAGE magnetometer network: Years 1993-2003 examined, J. Geophys. Res. Space Phys., 114, A05204. https://doi.org/10.1029/2008JA013682

Thiteridge, J.E. (1995). Winds in the Ionosphere-A Review, J. Atmos. Terr. Phys., 57, 14, 1681-1714. https://doi.org/10.1016/0021-9169(95)00091-F

Tornatore, V., C. Cesaroni, M. Pezzopane, M.M. Alizadeh and H. Schuh (2021). Performance evaluation of VTEC GIMs for regional applications during different solar activity periods, using RING TEC values, Rem. Sens., 13, 8, 1470. https://doi.org/10.3390/rs13081470

Tozzi, R., P. De Michelis, I. Coco and F. Giannattasio (2019). A preliminary risk assessment of geomagnetically induced currents over the Italian territory, Space Weather, 17, 46-58. https://doi.org/10.1029/2018SW002065

Tsurutani, B.T., A.J. Mannucci, B. Iijima, F.L. Guarnieri, W.D. Gonzalez, D.L. Judge, P. Gangopadhyay and J. Pap (2006). The extreme Halloween 2003 solar flares (and Bastille Day, 2000 Flare), ICMEs, and resultant extreme ionospheric effects: A review, Adv. Space Res., 37, 8, 1583-1588. https://doi.org/10.1016/j.asr.2005.05.114

Upper atmosphere physics and radiopropagation Working Group, Marcocci, C., M. Pezzopane E. Pica, V. Romano, D. Sabbagh, C. Scotto and E. Zuccheretti (2020a). Electronic Space Weather upper atmosphere database (eSWua) – HF data, version 1.0. Istituto Nazionale di Geofisica e Vulcanologia (INGV). https://doi.org/10.13127/eswua/hf

Upper atmosphere physics and radiopropagation Working Group, Cossari, A., G. Fontana, C. Marcocci, S. Pau, M. Pezzopane, E. Pica and E. Zuccheretti (2020b). Electronic Space Weather upper atmosphere database (eSWua) – HF validated data (Version 1.0). Istituto Nazionale di Geofisica e Vulcanologia (INGV). https://doi.org/10.13127/eswua/hfvalidated

Upper atmosphere physics and radiopropagation Working Group, Cesaroni, C., G. De Franceschi, C. Marcocci, E. Pica, V. Romano and L. Spogli (2020c). Electronic Space Weather upper atmosphere database (eSWua) – GNSS scintillation data, version 1.0. Istituto Nazionale di Geofisica e Vulcanologia (INGV). https://doi.org/10.13127/eswua/gnss

Upper Atmosphere Physics And Radiopropagation Working Group, Cesaroni, C., C. Marcocci, E. Pica and L. Spogli (2020d). Electronic Space Weather upper atmosphere database (eSWua) – Total Electron Content (TEC) data, version 1.0. Istituto Nazionale di Geofisica e Vulcanologia (INGV). https://doi.org/10.13127/eswua/tec

Watson, C. and N.M. Pedatella (2018). Climatology and characteristics of medium-scale F region ionospheric plasma irregularities observed by COSMIC radio occultation receivers, J. Geophys. Res. Space Phys., 123, 10, 8610-8630. https://doi.org/10.1029/2018JA025696

Wei, Y., B. Zhao, G. Li and W. Wan (2015). Electric field penetration into Earth' ionosphere: A brief review for 2000-2013, Sci. Bull., 60, 8, 748-761. https://doi.org/10.1007/s11434-015-0749-4

Wernik, A.W., J.A. Secan and E.J. Fremouw (2003). Ionospheric irregularities and scintillation, Adv. Space Res., 31, 4, 971-981. https://doi.org/10.1016/S0273-1177(02)00795-0

Wood, A.G., L. Alfonsi, L.B. Clausen, Y. Jin, L. Spogli, J. Urbář, J.T. Rawlings, I.C. Whuttaker, G.D. Dorrian, P. Høeg, D. Kotova, C. Cesaroni, A. Cicone, J. Miedzik., E. Gierlach, P. Kochanska, P. Wojtkiewica, G. Shahtahmassebi and W.J. Miloch (2022). Variability of ionospheric plasma: Results from the ESA Swarm mission, Space Sci. Rev., 218, 6, 52. https://doi.org/10.1007/s11214-022-00916-0

Wright, J.W. (1960). A model of the F region above hmaxF2, J. Geophys. Res., 65, 1, 185-191. https://doi.org/10.1029/JZ065i001p00185

Yang, Z. and Z. Liu (2016). Correlation between ROTI and Ionospheric Scintillation Indices using Hong Kong low-latitude GPS data, GPS Sol., 20, 815-824. https://doi.org/10.1007/s10291-015-0492-y

Yizengaw, E. and K. Groves (2018). Longitudinal and seasonal variability of equatorial ionospheric irregularities and electrodynamics, Space Weather, 16, 8, 946-968. https://doi.org/10.1029/2018SW001980

Yeh, K.C. and C.H. Liu (1982). Radio wave scintillations in the ionosphere, in proceedings of the IEEE, 70, 4, 324-360. 10.1109/PROC.1982.12313

Zuccheretti, E., G. Tutone, U. Sciacca, C. Bianchi and J.A. Baskaradas (2003). The new AIS-INGV digital ionosonde, Annals of Geophysics, 46, 647-659, https://doi.org/10.4401/ag-4377

***CORRESPONDING AUTHOR: Luca SPOGLI**,
Istituto Nazionale di Geofisica e Vulcanologia, Rome, Italy
e-mail: luca.spogli@ingv.it